LC-PHSM-2004-006
March 2004

Study of Higgs Boson Pair Production at Linear Collider

K. Desch[a], T. Klimkovich [a,b], T. Kuhl[b], A. Raspereza[b]

[a] *Universität Hamburg, Institut für Experimentalphysik Notkestrasse 85, D-22607 Hamburg, Germany.*

[b] *DESY, Notkestrasse 85, D-22607 Hamburg, Germany.*

Abstract

We study the potential of the TESLA linear collider operated at a center-of-mass energy of 500 to 1000 GeV for the measurement of the neutral Higgs boson properties within the framework of the MSSM. The process of associated Higgs boson production with subsequent decays of Higgs bosons into b-quark and τ-lepton pairs is considered. An integrated luminosity of 500 fb^{-1} is assumed at each energy. The Higgs boson masses and production cross sections are measured by reconstructing the $\mathrm{b\bar{b}b\bar{b}}$ and $\mathrm{b\bar{b}}\tau^+\tau^-$ final states. The precision of these measurements is evaluated in dependence of the Higgs boson masses. Under the assumed experimental conditions a statistical accuracy ranging from 0.1 to 1.0 GeV is achievable on the Higgs boson mass. The topological cross section $\sigma(\mathrm{e^+e^-} \to \mathrm{HA} \to \mathrm{b\bar{b}b\bar{b}})$ can be determined with the relative precision of 1.5 – 6.6 % and cross sections $\sigma(\mathrm{e^+e^-} \to \mathrm{HA} \to \mathrm{b\bar{b}}\tau^+\tau^-)$ and $\sigma(\mathrm{e^+e^-} \to \mathrm{HA} \to \tau^+\tau^-\mathrm{b\bar{b}})$ with precision of 4 – 30 %. Constraints on the Higgs boson widths can be set exploiting $\mathrm{b\bar{b}}\tau^+\tau^-$ channel. The 5σ discovery limit corresponds to the Higgs mass of around 385 GeV for the degenerate Higgs boson masses in the $\mathrm{HA} \to \mathrm{b\bar{b}b\bar{b}}$ channel at $\sqrt{s} = 800$ GeV with integrated luminosity of 500 fb^{-1}. The potential of the Higgs mass determination for the benchmark point SPS 1a for the process $\mathrm{HA} \to \mathrm{b\bar{b}b\bar{b}}$ at $\sqrt{s} =$ 1 TeV and luminosity 1000 fb^{-1} is investigated.

1 Introduction

Elucidating the mechanism of electroweak symmetry breaking will be one of the central tasks at a future linear e^+e^- collider. In the minimal Standard Model (SM) breaking of electroweak symmetry is provided by one Higgs doublet, which introduces an additional spin-0 particle, the Higgs boson [1]. Among models with an extended Higgs sector, two Higgs doublet models (2HDM) [2] are of particular interest, since this structure of the Higgs sector is required in the Minimal Supersymmetric Standard Model (MSSM) [3], the most seriously considered extension of the SM. The Higgs sector of the CP-conserving MSSM comprises the following physical states: two CP-even Higgs bosons, the lighter of which is denoted h and the heavier H, one CP-odd Higgs boson A and two charged bosons $H^{\pm}$. Two crucial parameters, which influence the Higgs boson phenomenology, are $\tan\beta$, the ratio of vacuum expectation values of the two Higgs doublets, and the angle α, which controls mixing in the CP-even sector.

The cross sections of the Higgs-strahlung and fusion processes, involving CP-even Higgs bosons,

$$e^+e^- \to hZ(HZ), \qquad e^+e^- \to h(H)\nu_e\bar{\nu}_e, \qquad e^+e^- \to h(H)e^+e^-, \tag{1}$$

are defined in terms of the strength of the Higgs couplings to weak bosons at tree level. These depend on the parameters α and β in the following way:

$$g_{hZZ,hWW} \sim \sin(\beta - \alpha), \qquad\qquad g_{HZZ,HWW} \sim \cos(\beta - \alpha). \tag{2}$$

In the MSSM, the set of the tree level couplings between neutral Higgs particles and weak bosons is extended by two additional couplings,

$$g_{hAZ} \sim \cos(\beta - \alpha), \qquad\qquad g_{HAZ} \sim \sin(\beta - \alpha). \tag{3}$$

As a consequence, in e^+e^- collisions, the Higgs-strahlung and fusion processes will be complemented by the associated Higgs boson pair production mechanisms:

$$e^+e^- \to hA(HA). \tag{4}$$

To fully explore the MSSM Higgs sector, the processes (4) must be studied, since they directly probe g_{hAZ} and g_{HAZ} trilinear couplings, provide access to the A boson properties and supplement the study of the CP-even Higgs boson properties via Higgs-strahlung and fusion mechanisms.

The study of the Higgs pair production process is motivated by a so-called decoupling limit of the MSSM in which the h boson approaches the properties of the SM Higgs boson. The closer MSSM scenario moves towards the decoupling limit the more difficult it becomes to distinguish the Higgs sector from the SM. In such a scenario the detection of heavier neutral Higgs bosons would be crucial for establishing an extended Higgs sector. The decoupling limit is approached relatively fast for large values of the H and A boson masses, $m_{\mathrm{A}}, m_{\mathrm{H}} > 200$ GeV, in a large portion of the MSSM parameter space. The distinct feature of this scenario is vanishing coupling of heavy CP-even Higgs boson to weak bosons, $\cos(\beta - \alpha) \rightarrow 0$. As a consequence, the H boson production via the fusion and Higgs-strahlung processes is significantly suppressed, whereas the cross section of the $\mathrm{e^+e^-} \rightarrow \mathrm{HA}$ process reaches its maximal value making associated heavy Higgs pair production a promising channel for the detection of the H and A bosons at a future linear $\mathrm{e^+e^-}$ collider. It should be also emphasized that in the decoupling limit the H and A bosons are almost degenerate in mass and have similar decay properties[1].

In this note the study of Higgs boson pair production at a future linear $\mathrm{e^+e^-}$ collider is presented. This analysis extends the previous studies [4, 5]. The analyzed topologies include the $\mathrm{b\bar{b}b\bar{b}}$ and $\mathrm{b\bar{b}}\tau^+\tau^-$ final states. In the following we will assume the $\mathrm{e^+e^-} \rightarrow \mathrm{HA}$ production process. However, this assumption does not restrict the generality of our study and the analyses developed in this note are applicable to the process $\mathrm{e^+e^-} \rightarrow \mathrm{hA}$ as well as to the processes of associated Higgs pair production in CP-violating MSSM scenarios where the neutral Higgs bosons are no longer CP eigenstates [6].

This note is organized as follows. In Section 2 the assumed experimental conditions and main features of the detector are discussed. Section 3 describes the simulation of the signal and the relevant background processes. In Section 4 the analysis tools, employed in our study, are briefly reviewed. Section 5 describes the analysis of the $\mathrm{b\bar{b}b\bar{b}}$ and $\mathrm{b\bar{b}}\tau^+\tau^-$ final states. In Section 6, we discuss the prospects of measuring the Higgs boson properties using the $\mathrm{b\bar{b}b\bar{b}}$ and $\mathrm{b\bar{b}}\tau^+\tau^-$ topologies. In Appendix the interpretation of this analysis is done for the SPS 1a benchmark point.

2 Experimental Conditions and Detector Simulations

The study is performed for a linear collider operated at a center-of-mass energies of 500 GeV to 1000 GeV and an event sample corresponding to an integrated luminosity of 500 fb^{-1}.

The detector used in the simulation follows the proposal for the TESLA

[1]These features will be exploited later on in our analysis.

collider presented in the TDR [4]. Studies were also performed in Asia and North America [7, 8]. The interaction region is surrounded by a tracker consisting of a multi-layered pixel micro-vertex detector (VTX) as the innermost part and a large time projection chamber (TPC) supplemented with additional silicon strip detector in the forward region (FTD) and two bands between VTX and TPC. In radial direction follow an electromagnetic calorimeter, a hadron calorimeter, the coils of a superconducting magnet and an instrumented iron flux return yoke. The solenoidal magnetic field is 4 Tesla.

The envisaged impact parameter resolution provided by the vertex detector is

$$\delta(IP_{r\phi,z}) \leq 5\mu m \oplus \frac{10\mu m\ GeV/c}{p\sin^{3/2}\theta}, \tag{5}$$

where p is the track momentum and θ is the polar angle. The overall central tracker momentum resolution is

$$\sigma\left(\frac{1}{p_t}\right) \leq 5 \cdot 10^{-5}\ [\ \mathrm{GeV}/c]^{-1}, \tag{6}$$

where p_t is the transverse momentum. To enable efficient separation of neutral and charged particles, highly granular electromagnetic and hadronic calorimeters are foreseen for the TESLA detector. Their energy resolutions are:

$$\frac{\sigma_{E_{el}}}{E_{el}} = \frac{10\%}{\sqrt{E_{el}}} \oplus 1\%, \qquad \frac{\sigma_{E_h}}{E_h} = \frac{50\%}{\sqrt{E_h}} \oplus 4\%, \tag{7}$$

where E_{el} and E_h are the energies measured for electrons and hadrons in the corresponding calorimeters. The polar angle coverage of the central tracker maintaining the resolution is $|\cos\theta| < 0.85$, above this range the tracking resolution deteriorates. The electromagnetic and hadron calorimeters cover $|\cos\theta| < 0.996$ maintaining the resolution over the whole angular range.

The detector response is simulated with parametric fast simulation program SIMDET [9]. Beamstrahlung is accounted for using CIRCE [10].

The event reconstruction is done in terms of energy flow objects. First, tracks are measured with tracking system and associated to calorimetric clusters to define charged energy flow objects (electrons, muons and charged hadrons). Since momentum measurement with tracking system is much more accurate than direction and energy measurements with calorimeters, the tracking information is used for estimation of the four-momentum of the charged objects. Calorimetric clusters with no associated tracks are regarded as neutral energy flow objects (photons and neutral hadrons). Measurements of the four-momentum of neutral objects are solely based on the calorimetric information.

3 Physics Processes and Monte Carlo Samples

Samples of $e^+e^- \to HA$ events are generated for several Higgs boson mass hypotheses with PYTHIA 6.2 [11], including initial state radiation. The tree level cross section of the HA production is related to the Higgs-strahlung cross section in the SM, σ_{HZ}^{SM}, in the following way [2]:

$$\sigma_{HA} = g_{HAZ}^2 \bar{\lambda}_{HA} \sigma_{HZ}^{SM}, \tag{8}$$

where

$$\bar{\lambda}_{HA} = \frac{\lambda_{HA}^{3/2}}{\lambda_{HZ}^{1/2}[12m_Z^2/s + \lambda_{HZ}]} \tag{9}$$

accounts for the correct suppression of the P-wave cross section near the kinematic threshold. The quantity $\lambda_{ij} = [1-(m_i+m_j)^2/s][1-(m_i-m_j)^2/s]$ is the usual momentum factor of the two particle phase space. The Higgs-strahlung cross section in the SM is computed using the program HPROD [12].

For the case of maximal allowed g_{HAZ} coupling, $\sin(\beta-\alpha) = 1$, which is assumed for these studies, signal cross sections are given in Table 1. The branching fractions of the Higgs bosons into b-quarks and τ-lepton pairs are set to their typical values in the MSSM : $Br(H \to b\bar{b}) = Br(A \to b\bar{b}) = 90\%$, $Br(H \to \tau\tau) = Br(A \to \tau\tau) = 10\%$.

For the background estimation, the following processes are generated using PYTHIA 6.2: $e^+e^- \to WW$, $e^+e^- \to ZZ$, $e^+e^- \to q\bar{q}$[2], $e^+e^- \to Ze^+e^-$ and $e^+e^- \to We\nu$. The cross sections for the most important background processes are given in Table 2.

4 Analysis tools

4.1 B-tagging

Identification of b-quarks plays a crucial role in this analysis. Efficient tagging of jets containing heavy flavour hadrons will be achieved with a highly granular micro-vertex detector, allowing for precise reconstruction of track parameters in the vicinity of the primary interaction point.

[2]The $e^+e^- \to t\bar{t}$ events are also taken into account

The procedure of tagging b-jets exploits information from the single track as well as secondary vertex information. Secondary vertices are searched within jets using the package ZVTOP [13] developed for the SLD experiment, where tracks are described as probability tubes and seed vertices are defined as regions where these tubes overlap. Afterwards an attempt is made to assign additional tracks by an iterative procedure. For each found vertex the invariant total mass and momentum are calculated from the four-momenta of energy flow objects assigned to the vertex. Three dimensional decay length and decay length significance are also computed.

For a jet flavour separation a neural network is developed. The detailed description of the neural network implementation for the full simulation of the TESLA detector with the BRAHMS program [14] can be found in [15]. Three different neural networks are introduced for jets with no, one and more than one secondary vertices found. For jets without secondary vertex, the impact parameter joint probability [16] and the two highest impact parameter significances are used as inputs for the neural network. If jet contains at least one secondary vertex, an additional information, including vertex masses, momenta, decay lengths and decay length significances, is fed into the neural network.

The neural networks are trained on event samples simulated with SIMDET using the same variables and jet classification as in BRAHMS. For the analysis, a jet-wise tag, referred hereafter as jet b-tag variable, is used. For a jet with neural network output x it is defined as

$$B(x) = \frac{f_b(x)}{f_b(x) + f_{udsc}(x)}, \tag{10}$$

where $f_b(x)$ and $f_{udsc}(x)$ are probability density functions of neural network output in a samples of b– and udsc–jets, respectively. Tagging of c-jets proceeds in a similar way.

Fig. 1 shows b-tag and c-tag purity versus efficiency curves for $\mathrm{Z} \to \mathrm{q\bar{q}}$ events simulated at a center-of-mass energy of $\sqrt{s} = 91.2\,\mathrm{GeV}$. Results obtained with SIMDET and BRAHMS are compared in this figure. The c-tag performance agrees within 5% over the entire range of efficiency. Some discrepancy in modelling of the b-tag is observed in the region of high efficiency and low purity. This discrepancy occurs due to not adequate modelling of the resolution tails in the impact parameter joint probability distribution by SIMDET. However, both $\mathrm{b\bar{b}b\bar{b}}$ and $\mathrm{b\bar{b}}\tau^+\tau^-$ analyses impose b-tag requirements strong enough not to be sensitive to this discrepancy. Some flavour tag related systematic studies have been performed. It has been found that the b-tag performance is nearly independent of the center-of-mass energy in the range from $\sqrt{s} = 91.2\,\mathrm{GeV}$ to $\sqrt{s} = 500\,\mathrm{GeV}$. Furthermore, possible changes in micro-vertex detector configuration are found to have marginal impact on the b-tag performance. For example, removing innermost silicon layer changes the selection efficiency by not more than 5%. These studies confirm the stability of b-tagging. However, c-tag and e.g. b-quark charge tagging are depending on the innermost layer.

4.2 Kinematic Fit

The mass resolution of the reconstructed Higgs bosons is improved by means of a kinematic fit. In the $\mathrm{b\bar{b}b\bar{b}}$ analysis, conservation of four-momentum is required, leading in total to four constraints. In the case of the $\mathrm{b\bar{b}}\tau^+\tau^-$ topology, the energies of τ-leptons are not measurable due to undetectable neutrinos. However, the flight direction of highly boosted τ-leptons can be approximated with good accuracy by the direction of the total momentum of its visible decay products. Exploiting this approximation together with the the four-momentum conservation requirement, we arrive at a two constraint fit.

The jet angular and momentum resolution functions and the angular resolution of τ-leptons are derived from Monte Carlo studies. The kinematic fit is performed using the code developed by DELPHI [17]. For the samples of the $\mathrm{HA} \to \mathrm{b\bar{b}b\bar{b}}$ and $\mathrm{HA} \to \mathrm{b\bar{b}}\tau^+\tau^-$ events with $(m_\mathrm{H}, m_\mathrm{A})$ = (150,100) GeV, the performance of the kinematic fit is illustrated in Fig. 2 and 3, respectively.

5 Analysis Procedures

5.1 The $\mathrm{HA} \to \mathrm{b\bar{b}b\bar{b}}$ Channel

Events of the $\mathrm{b\bar{b}b\bar{b}}$ topology are characterized by four high multiplicity hadronic jets, containing decay products of b-hadrons. A cut-based technique is employed to separate signal from background. Selection criteria are optimized separately for 500 GeV and 800 GeV center-of-mass energies. Each event is required to pass the following cuts:

1. Total energy deposited in the detector, the visible energy $\mathrm{E_{vis}}$, must be greater than 340 GeV (600 GeV) for 500 GeV (800 GeV) center-of-mass energies.

2. Each event is forced into four jets using the DURHAM algorithm [18] and the number of tracks per jet is required to be greater than three.

3. To separate centrally produced H and A bosons from the WW and ZZ events, peaking in forward/backward direction, we apply a cut on the polar angle of the thrust vector [11], $|\cos\theta_T| < 0.8$.

4. Further suppression of the WW and ZZ backgrounds is achieved by requiring the event thrust value to be less than 0.88.

5. Two fermion background is suppressed by applying a cut on the DURHAM jet resolution parameter, for which the event changes from four to three jets, $\log_{10} y_{34} \geq -2.9$.

6. High multiplicity six-jet events originating from the $\mathrm{e^+e^-} \to \mathrm{t\bar{t}}$ production are reduced by requiring the number of enflow (energy flow) objects in the event to be less than 130. This cut is applied only at $\sqrt{s}$ = 500 GeV.

7. The background from $\mathrm{e^+e^-} \to \mathrm{t\bar{t}}$ events is further reduced by applying a cut on the jet resolution parameter, for which the event changes from six to five jets, $\log_{10} y_{56} \leq$ -3.1 (-2.8) at $\sqrt{s}$ = 500 GeV (800 GeV).

8. Finally, we make use of the b-tag information to enhance the purity of the selected event sample. First, the b-tag variable for each jet is calculated as described in Section 4. The four b-tag variables are sorted in descending order, $B_1 > B_2 > B_3 > B_4$. Two quantities B_{12}, B_{34} are then defined as

$$B_{12} = \frac{B_1 B_2}{B_1 B_2 + (1 - B_1)(1 - B_2)},$$

$$B_{34} = \frac{B_3 B_4}{B_3 B_4 + (1 - B_3)(1 - B_4)}.$$

   The value of B_{12} has to be greater than 0.75 (0.6) at $\sqrt{s}$ = 500 GeV (800 GeV). The value of B_{34} is required to be greater than 0.05 independent of the center-of-mass energy.

The numbers of expected signal and background events, retained after selection, and signal efficiency for the example points with (m_H,m_A) = (150,100) GeV at $\sqrt{s}$ = 500 GeVand (m_H,m_A) = (300,250) at $\sqrt{s}$ = 800 GeVare presented in Tables 3, 4. Fig. 4 and 5 show the distributions of the selection variables for the different sources of background and for the signal at $\sqrt{s}$ = 500 GeV. The cutflow table for this case shows that such cuts like those on visible energy, number of tracks per jet, polar angle on the thrust vector and b-tag cuts are very effective to separate signal from the background. Especially should be stressed that after all kinematic selection i.e. before b-tag cuts the signal efficiency is 54% while the background is drastically reduced (1.6% from the initial value). After b-tag cuts only 1.3% of the background events, left after kinematic selection, remains, while the signal efficiency is 43%. This confirms, that the new tool for b-tagging is very powerful. The signal efficiencies, number of signal events and total background for different Higgs boson masses after selection cuts are given in Table 5.

Events accepted in the final sample are subjected to a 4C kinematic fit. For each of the three possible di-jet pairings, the di-jet mass sum and the di-jet mass difference are reconstructed. For the example point the mass sum and the mass difference presented in Fig. 2 show that due to the kinematic fit the mass reconstruction resolution can be improved significantly.

5.2 The HA $\rightarrow \mathrm{b\bar{b}}\tau^+\tau^-, \tau^+\tau^-\mathrm{b\bar{b}}$ Channels

The signature of the $\mathrm{b\bar{b}}\tau^+\tau^-$ final state consists of two high-multiplicity hadronic jets enriched with the decay products of b-hadrons and two low-multiplicity jets initiated by τ-leptons.

Initially, a preselection of high-multiplicity events compatible with the four-jet topology is applied. Events are required to fulfill the following criteria.

1. The leptonic and two photon events are rejected by applying lower cut on the number of energy flow objects, $\mathrm{N_{enflow}} > 30$.

2. Genuine six-jet events, resulting from the $\mathrm{e^+e^-} \rightarrow \mathrm{t\bar{t}}$ production and characterized by very large particle multiplicity, are partially suppressed by an upper cut on the number of energy flow objects, $\mathrm{N_{enflow}} < 120$.

3. The visible energy $\mathrm{E_{vis}}$ must be greater than 250 GeV (400 GeV) at $\sqrt{s}$ = 500 GeV (800 GeV). This cut suppresses background processes characterized by large missing energy: $\mathrm{ZZ} \rightarrow \mathrm{q\bar{q}}\nu\bar{\nu}$ events, radiative returns to the Z resonance with a photon escaping into the beam pipe and $\mathrm{e^+e^-} \rightarrow \mathrm{We}\nu$, $\mathrm{e^+e^-} \rightarrow \mathrm{Ze^+e^-}$ processes with electrons escaping undetected in the forward direction. An upper cut $\mathrm{E_{vis}} < 500$ GeV (760 GeV) at $\sqrt{s}$ = 500 GeV (800 GeV) allows partial rejection of the fully hadronic $\mathrm{WW} \rightarrow \mathrm{q\bar{q}q\bar{q}}$ and $\mathrm{ZZ} \rightarrow \mathrm{q\bar{q}q\bar{q}}$ events without significant loss in the signal efficiency.

4. The event thrust value has to be less than 0.95. This cut disentangles more spheric HA events from the WW, ZZ and $\mathrm{q\bar{q}}$ backgrounds in which

the high boost of the final state bosons/quarks results in large values of the event thrust.

5. To separate centrally produced H and A bosons from the WW and ZZ processes in which weak bosons tend to peak in the forward/backward directions, a cut on the polar angle of the thrust vector, $|\cos\theta_T| < 0.9$, is applied.

6. The event is discarded if it contains an e^+e^- or $\mu^-\mu^+$ pair with invariant mass compatible with the Z mass within 5 GeV. This cut suppresses the $ZZ \to q\bar{q}\ell^+\ell^-$ background.

Events satisfying these criteria are resolved into four-jet topology and τ-lepton identification is performed. Two identification categories for τ-leptons are introduced. A low multiplicity jet is assigned to the first category if it fulfills one of the following tight conditions:

- A jet contains only one charged track, identified as an electron or muon. No neutral clusters are assigned to the jet.

- A jet contains one charged track, identified as hadron, and not more than four neutral clusters (one-prong hadronic decay of τ-lepton).

- A jet contains three charged tracks with unit total charge and has not more than two neutral calorimetric clusters (three-prong hadronic decay of τ-lepton).

To enhance the acceptance of signal events, the second identification category, imposing looser criteria, is introduced. According to these criteria, a jet is identified as τ-lepton if it has not more than two charged tracks and less than five neutral clusters.

An event is accepted if at least one of the low multiplicity jets satisfies the tight identification criteria. Signal efficiencies and numbers of signal and background events remaining after preselection are given in Table 6.

In the next step, events are selected into the final sample by means of a binned likelihood technique. The signal likelihood, L_{HA} is built from the following variables:

- event thrust, T;

- the polar angle of the thrust vector, $\cos\theta_T$;

- minimal opening angle between any two of the four jets;

- b-tag variables of the two hadronic jets, B_1 and B_2 (hadronic jets are ordered by their energy);
- missing energy;
- number of energy flow objects, N_{enflow}.

Fig. 6 and 7 show the distributions of these variables. The distribution of L_{HA} is shown in Fig. 8 for $(m_{\mathrm{H}},m_{\mathrm{A}})$ = (150,100) GeV at $\sqrt{s}$ = 500 GeV. An event is accepted in the final sample if the value of L_{HA} is greater than certain threshold optimized separately for each Higgs boson mass hypothesis considered to yield maximal significance of the signal. The number of signal and background events and the signal efficiencies after final selection are given in Table 7. Signal efficiency ranges between 30 and 45%, and the number of background events contributing to the final sample between 2000 and 6000, depending on the Higgs mass.

For events accepted in the final sample, the di-jet and di-tau invariant masses are reconstructed exploiting the 2C kinematic fit, described in Section 4.

6 Results

In the final step of the analysis, the spectra of the di-jet mass sum and difference, obtained in the HA $\rightarrow$ $\mathrm{b\bar{b}b\bar{b}}$ channel, and distributions of the di-jet and di-tau masses, reconstructed in the HA $\rightarrow$ $\mathrm{b\bar{b}}\tau^+\tau^-$, $\tau^+\tau^-\mathrm{b\bar{b}}$ channels, are used to determine Higgs boson properties.

6.1 Cross section and Mass

First, the analysis is performed assuming that the natural widths of the Higgs bosons are small compared to the detector resolution. As an example Fig. 9 shows the distributions of the di-jet mass sum and di-jet mass difference obtained after selection cuts and kinematic fit in the HA $\rightarrow$ $\mathrm{b\bar{b}b\bar{b}}$ channel for the Higgs boson mass hypothesis of $(m_{\mathrm{H}},m_{\mathrm{A}})$ = (300,250) GeV at $\sqrt{s}$ = 800 GeV. Three entries per event contribute to these distributions, corresponding to three possibilities to pair jets in the four-jet events. Two entries form a so-called combinatorial background. Fig. 10 demonstrates the final di-jet mass sum and di-jet mass difference after the cut on the di-jet mass difference sum, respectively, as indicated by arrows in Fig. 9. The signal efficiencies, number of signal events and total background for different Higgs boson masses after cuts on di-jet mass sum and difference are given in Table 5.

The mass distributions are fitted separately with the signal normalization, the sum and the difference of the Higgs boson masses as free parameters. The shapes of the signal distributions are parametrised using high statistics signal samples. Background is approximated with a polynomial function. From the fit, the sum and the difference of the Higgs boson masses and errors on these quantities are determined. The di-jet mass sum and difference are found to be weakly correlated quantities. Hence, the statistical errors on the masses of the Higgs bosons can be calculated as follows:

$$\delta m_{\mathrm{H}} = \delta m_{\mathrm{A}} = \frac{1}{2}\sqrt{(\delta\Sigma^2 + \delta\Delta^2)},$$

where $\delta\Sigma$ and $\delta\Delta$ are statistical uncertainties in determination of the Higgs boson mass sum and difference. The error on the topological cross section is calculated as

$$\delta\sigma/\sigma = \sqrt{N_S + N_B}/N_S.$$

The notations N_S and N_B stand for the number of background and signal entries within the windows in the di-jet mass sum and di-jet mass difference distributions, where the signal is accumulated. The boundaries of these windows are optimized to yield a minimal relative error on the topological cross section.

In the $\mathrm{HA} \to \mathrm{b\bar{b}}\tau^+\tau^-$, $\tau^+\tau^-\mathrm{b\bar{b}}$ channels, in the case of large mass splitting between Higgs bosons, the signal exhibits itself as two peaks in the reconstructed di-jet and di-tau mass spectra as illustrated in Fig. 11. The spectra are fitted simultaneously with the superposition of background and signal distributions. The fit is performed with four free parameters : two normalization factors for the $\mathrm{HA} \to \mathrm{b\bar{b}}\tau^+\tau^-$ and $\mathrm{HA} \to \tau^+\tau^-\mathrm{b\bar{b}}$ samples and two Higgs boson masses. Background distribution is assumed to be well measured and therefore fixed. The shapes of signal peaks are parametrised using high statistics MC samples. When H and A are degenerate in mass, signal distributions overlap and the contributions from the $\mathrm{HA} \to \mathrm{b\bar{b}}\tau^+\tau^-$ and $\mathrm{HA} \to \tau^+\tau^-\mathrm{b\bar{b}}$ samples cannot be disentangled. To stabilize the fitting procedure we assume that the numbers of the $\mathrm{HA} \to \mathrm{b\bar{b}}\tau^+\tau^-$ and $\mathrm{HA} \to \tau^+\tau^-\mathrm{b\bar{b}}$ events, selected into the final sample, are equal. This assumption is validated by the properties of the decoupling limit. As was mentioned in the introductory section, in the decoupling limit the H and A bosons have almost identical properties: $m_{\mathrm{H}} \approx m_{\mathrm{A}}$, $\mathrm{Br}(\mathrm{H} \to \mathrm{b\bar{b}}) \approx \mathrm{Br}(\mathrm{A} \to \mathrm{b\bar{b}})$, $\mathrm{Br}(\mathrm{H} \to \tau\tau) \approx \mathrm{Br}(\mathrm{A} \to \tau\tau)$, $\Gamma_{\mathrm{H}} \approx \Gamma_{\mathrm{A}}$. Consequently, the $\mathrm{HA} \to \mathrm{b\bar{b}}\tau^+\tau^-$ and $\mathrm{HA} \to \tau^+\tau^-\mathrm{b\bar{b}}$ events are expected to contribute equally to the final selected sample. This reduces the number of free parameters to three : a common normalization factor for the two signal samples and two Higgs boson masses. As an example, Fig. 12 shows the result of the fit for (m_{H},m_{A}) = (300,300) GeV.

Table 8 summarizes the statistical accuracy of the mass measurements for the HA $\to$ b$\bar{\text{b}}$b$\bar{\text{b}}$ and HA $\to$ b$\bar{\text{b}}\tau^+\tau^-, \tau^+\tau^-b\bar{\text{b}}$ channels and their combination. The statistical accuracy of the combined mass measurement is $\sim$ 100 MeV for the Higgs pair production far above kinematic threshold and degrades to $\sim$ 1 GeV with aproaching kinematic limit. At the same time the statistical errors for the $\sqrt{s} = 800$ GeV are in general twice as bigger than those for the 500 GeV for the both channels. The combination of the two channels helps to improve the mass determination accuracy.

The statistical uncertainty on the topological cross sections is reported in Table 9. In the HA $\to$ b$\bar{\text{b}}$b$\bar{\text{b}}$ channel, the topological cross sections can be measured with relative precision between 1.5 and 6.6% while in the HA $\to$ b$\bar{\text{b}}\tau^+\tau^-, \tau^+\tau^-b\bar{\text{b}}$ channels between 5 to 30%.

A big part of SUSY parameter space leads to degenerate H and A Higgs boson masses. For this case the discovery significance as a function of m_H (=m_A) (Fig. 13) is calculated for the HA $\to$ b$\bar{\text{b}}$b$\bar{\text{b}}$ channel at $\sqrt{s} = 800$ GeV. Approaching the kinematic limit, the significance drops below 5σ between 380 GeV to 390. The whole range of the significances for the Higgs masses is from 28.2 to 3.4. The 5σ discovery reach and η^2 as a function of m_H (=m_A) where η^2 is assumed e$^+$e$^-$ $\to$ HA cross section relative to that for $\sin^2(\beta - \alpha) = 1$ (as shown in Fig. 13).

6.2 Width

We utilize the HA $\to$ b$\bar{\text{b}}\tau^+\tau^-, \tau^+\tau^-b\bar{\text{b}}$ channels to measure the Higgs boson widths. Fig. 14 illustrates the impact of the natural widths of the Higgs bosons on the reconstructed di-jet and di-tau mass spectra. We consider separately two cases :

1. large mass splitting between H and A,
2. mass degeneracy.

In the first case, the strategy of the measurement is the following. The masses of Higgs bosons are fixed to the values measured in the HA $\to$ b$\bar{\text{b}}$b$\bar{\text{b}}$ channel. The reconstructed di-jet and di-tau mass line shapes are parametrised as a function of Γ_H and Γ_A using MC samples of the HA $\to$ b$\bar{\text{b}}\tau^+\tau^-$ and HA $\to \tau^+\tau^-$b$\bar{\text{b}}$ events generated with different Higgs boson widths. A simultaneous log-likelihood fit of the parametrised mass line shapes to the actual reconstructed di-jet and di-tau mass distributions is performed with four free parameters : Γ_H, Γ_A and two normalization factors for the HA $\to$ b$\bar{\text{b}}\tau^+\tau^-$ and HA $\to \tau^+\tau^-$b$\bar{\text{b}}$ samples. Fig. 15 shows the dependence of the log-likelihood on the probed Higgs boson widths for the case of $\Gamma_\text{H} = \Gamma_\text{A} =$

5 GeV and ($m_{\rm H}$,$m_{\rm A}$) = (200,150) GeV at $\sqrt{s}$ = 500 GeV. The dependence is shown for the case when only di-jet mass or di-tau mass spectrum are fitted and for the simultaneous fit to the two distributions. The feasible accuracies of the width measurements for three representative Higgs boson mass hypotheses are given in Table 10. The precision on the width determination ranges from 600 MeV to 4.0 GeV.

In the case of very close Higgs boson masses, the broadening of the signal peak in the mass distributions can be caused by two factors : the finite natural widths of the Higgs bosons and non-zero mass difference, $\delta M = m_{\rm H} - m_{\rm A}$. The width measurement in this case proceeds as follows. The sum of the Higgs boson masses is fixed to the value measured in the HA $\to$ b$\bar{\rm b}$b$\bar{\rm b}$ channel, $m_{\rm H} + m_{\rm A} = 2M$. From the HA $\to$ b$\bar{\rm b}\tau^+\tau^-$ and HA $\to \tau^+\tau^-$b$\bar{\rm b}$ MC samples with $\Gamma_{\rm H} = \Gamma_{\rm A} = 0$ GeV, the experimental mass resolution functions $R_{bb,\tau\tau}(x)$ are derived, which approximate the reconstructed di-jet and di-tau mass distributions in the limit of infinitely small Higgs widths. To ensure stability of the fitting procedure, the H and A boson are assumed to have identical decay properties, Br(H $\to$ b$\bar{\rm b}$) = Br(A $\to$ b$\bar{\rm b}$), Br(H $\to \tau\tau$) = Br(A $\to \tau\tau$), $\Gamma_{\rm H} = \Gamma_{\rm A} = \Gamma$, as expected in the decoupling limit. The distributions of the invariant di-jet and di-tau masses are fitted simultaneously with the functions

$$\begin{aligned} F_{bb,\tau\tau}(x) &= B_{bb,\tau\tau}(x) + N \cdot BW(x, M \pm \delta M/2, \Gamma) \otimes R_{bb,\tau\tau}(x) + \\ & \qquad N \cdot BW(x, M \mp \delta M/2, \Gamma) \otimes R_{bb,\tau\tau}(x) \end{aligned}$$

The fitting functions consist of three terms. The first one, $B_{bb,\tau\tau}(x)$, describes the background spectrum. The other two describe two signal distributions and represent the convolution of the Breit-Wigner function

$$BW(x, M, \Gamma) = \frac{xM\Gamma}{(x^2 - M^2)^2 + M^2\Gamma^2}$$

with the experimental resolution functions $R_{bb,\tau\tau}(x)$. The fit is performed with the common normalization factor, N, the Higgs boson width, Γ, and the Higgs boson mass difference, δM, as free parameters. The Higgs width errors obtained from the fitting procedure are presented in Table 11 for three representative Higgs mass hypotheses. The precision on the width determination ranges from 1 GeV to 4.5 GeV.

7 Conclusion

We examined the potential of a future linear collider detector for the determination of the MSSM Higgs boson properties exploiting associated Higgs boson pair production followed by the Higgs decays to b-quarks and τ-leptons. It is shown that combining the $\mathrm{HA} \to \mathrm{b\bar{b}b\bar{b}}$ and $\mathrm{HA} \to \mathrm{b\bar{b}}\tau^+\tau^-, \tau^+\tau^-\mathrm{b\bar{b}}$ channels the Higgs boson masses can be measured with an accuracy of up to several hundred MeV for Higgs pair production far above the kinematic threshold. The precision deteriorates to about 1 GeV with approaching the kinematic threshold. The topological cross section $\sigma(\mathrm{e^+e^-} \to \mathrm{HA} \to \mathrm{b\bar{b}b\bar{b}})$ can be measured with a relative precision varying between 1.5 and 6.6%. The error on the topological cross sections $\sigma(\mathrm{e^+e^-} \to \mathrm{HA} \to \mathrm{b\bar{b}}\tau^+\tau^-)$ and $\sigma(\mathrm{e^+e^-} \to \mathrm{HA} \to \tau^+\tau^-\mathrm{b\bar{b}})$ is estimated to range between 4 and 30%. Moderate constraints on the Higgs boson widths can be set from the analysis of the reconstructed di-jet and di-tau mass spectra in the $\mathrm{HA} \to \mathrm{b\bar{b}}\tau^+\tau^-$ and $\mathrm{HA} \to \tau^+\tau^-\mathrm{b\bar{b}}$ channels.

The 5σ discovery limit corresponds to the Higgs mass of around 385 GeV for the degenerate Higgs boson masses in the $\mathrm{HA} \to \mathrm{b\bar{b}b\bar{b}}$ channel at $\sqrt{s}$ = 800 GeV with integrated luminosity of 500 fb^{-1}.

A SPS 1a

The present analysis is applied to one of the so-called benchmark points SPS 1a for SUSY searches [19]. SPS 1 is a typical mSUGRA scenario which consists of a point with an intermediate value of $\tan\beta$ and a model line attached to it (SPS 1a) and of a "typical" mSUGRA point with relatively high $\tan\beta$ (SPS 1b). The parameters for the SPS 1a point are m_0 = 100 GeV, $m_{1/2}$ = 250 GeV, A_0 = -100 GeV, $\tan\beta = 10$, $\mu > 0$. For this point the Higgs masses are m_{h^0} = 113.7 GeV, m_{A^0} = 394.65 GeV, m_{H^0} = 394.9, $m_{H^\pm}$ = 403.6 GeV according to the Hdecay and Feynhiggsfast programs [20, 21].

The analysis is done for the center-of-mass energy of $\sqrt{s}$ = 1 TeV, at which the cross section for the process $e^+e^- \to$ HA is 2.5 fb. The luminosity assumed is 1000 fb^{-1}. The branching ratio for the H (A) Higgs boson to $b\bar{b}$ is 0.64 (0.40), Γ_{tot} = 0.785 GeV (1.251 GeV).

The results presented in Fig. 16 are the mass sum and the mass difference after the selection cuts, kinematic fit and the final cuts for the mass difference and the mass sum respectively. The masses can be measured with precision of 1.3 GeV. The signal efficiency is 29% after selection cuts and 24% after cuts on di-jet mass sum and difference. The cross section can be measured with the relative uncertainty of 9%.

References

[1] P.W. Higgs, Phys. Lett. **12** (1964) 132, Phys. Rev. Lett. **13** (1964) 508 and Phys. Rev. **145** (1966) 1156 ;
F. Englert and R. Brout, Phys. Rev. Lett. **13** (1964) 321;
G.S. Guralnik, C.R. Hagen and T.W.B. Kibble, Phys. Rev. Lett. **13** (1964) 585.

[2] J.F. Gunion, H.E. Haber, G. Kane, S. Dawson, "The Higgs Hunter's Guide", Addison Wesley, 1990.

[3] H.P. Nilles, Phys. Rep. **110** (1984) 1;
H.E. Haber and G.L. Kane, Phys. Rep. **117** (1985) 75;
R. Barbieri, Riv. Nuovo Cim., **11 n°4** 1.

[4] T. Behnke, S. Bertolucci, R.-D. Heuer, R. Settles, "TESLA : The Superconducting Electron-Positron Linear Collider with an Integrated X-Ray Laser Laboratory. Technical Design Report, Part IV : A Detector for TESLA", DESY 2001-011 and ECFA 2001-209 (2001).

[5] A. Andreazza, C. Troncon, "Study of HA Production in e^+e^- Collisions at $\sqrt{s} = 800$ GeV". DESY-123-E, p. 417.

[6] A. Pilaftsis and C.E.M. Wagner, Nucl. Phys. B553 (1999) 3.

[7] S. Kiyoura, S. Kanemura, K. Odagiri, Y. Okada, E. Senaha, S. Yamashita and Y. Yasui, arXiv:hep-ph/0301172.

[8] T. Abe et al., "Linear Collider Physics Resource Book for Snowmass 2001", BNL-52627, CLNS 01/1729, FERMILAB-Pub-01/058-E, LBNL-47813, SLAC-R-570, UCRL-ID-143810-DR, LC-REV-2001-074-US.

[9] SIMDET V4.0, M. Pohl and H.J. Schreiber, "SIMDET : a Parametric Monte Carlo for a TESLA Detector", DESY-02-061 LC-DET-2002-005 (2002).

[10] CIRCE V6, T. Ohl, Comp. Phys. Comm. **94** (1996) 53.

[11] T. Sjöstrand, L. Lonnblad, S. Mrenna, "PYTHIA 6.2: Physics and Manual", hep-ph/0108264.

[12] A. Djouadi, "HPROD: A Program for SM and MSSM Higgs Boson Production in e^+e^- Collisions",
http://w3.lpm.univ-montp2.fr/~djouadi/GDR/programs/hprod.html

[13] D. Jackson, Nucl. Instr. and Meth. **A388** (1997) 247.

[14] T. Behnke *et al.*, "BRAHMS : a Monte Carlo for a Detector at a 500/800 GeV Linear Collider", LC-TOOL-2001-005.

[15] S. Xella-Hansen, D.J. Jackson, R. Hawkings, C.J.S. Damerell, "Flavour Tagging Studies for the TESLA Linear Collider", LC-PHSM-2001-024.

[16] R. Barate et al. "A Measurement of R_b using a Lifetime-Mass Tag", CERN-PPE/97-017.

[17] N. Kjaer and R. Moller, "Reconstruction of invariant masses in multi-jet events", DELPHI Note 91-17 PHYS 88;
N. Kjaer, private communication.

[18] S. Catani, Yu.L. Dokshitzer, M. Olsson, G. Turnock and B.R. Webber, Phys. Lett. B269 (1991) 432.

[19] B.C. Allanach, M. Battaglia, G.A. Blair, M. Carena et al., hep-ph/0202233.

[20] A. Djouadi, J. Kalinowski, M. Spira, "Hdecay: a program for Higgs boson decays in the Standard Model and its supersymmetric extension", Comput. Phys. Commun. 108:56-74,1998; hep-ph/9704448.

[21] S. Heinemeyer, W. Hollik, G. Weiglein, "Feynhiggs and Feynhiggsfast: programs for higher order calculations in the neutral CP even Higgs boson sector of the MSSM", LC-TH-2001-065, KA-TP-5-2001, 2001. In 2nd ECFA/DESY Study 1998-2001 2393-2421.

$\sqrt{s}$ [GeV]	(m_{H},m_{A}) [GeV]	σ_{HA} [fb]
500	(150,100)	33.62
	(200,100)	25.30
	(250,100)	16.61
	(150,140)	28.39
	(150,150)	26.90
	(200,150)	18.85
	(250,150)	10.67
	(200,200)	11.35
800	(300,150)	10.55
	(290,200)	9.54
	(300,250)	7.49
	(300,300)	5.70
	(350,350)	2.23
	(400,150)	6.46
	(400,200)	5.17
	(400,250)	3.70

Table 1: Tree level cross sections σ_{HA} for $\mathrm{e^+e^-} \rightarrow$ HA expected for the Higgs boson mass hypotheses (m_{H},m_{A}) considered in the study. Numbers are given for $\sin^2(\beta-\alpha)$=1. Cross sections are calculated including ISR at center-of-mass energies of $\sqrt{s}$ = 500, 800 GeV.

Process	$\sigma \times BR$ [fb]	
	500 GeV	800 GeV
$\mathrm{t\bar{t}} \to \mathrm{W^+bW^-\bar{b}}$	$6.69 \cdot 10^2$	$1.65 \cdot 10^2$
$\mathrm{WW} \to \mathrm{q\bar{q}q\bar{q}}$	$4.13 \cdot 10^3$	$2.34 \cdot 10^3$
$\mathrm{WW} \to \mathrm{q\bar{q}}\ell\nu_\ell$	$3.88 \cdot 10^3$	$2.20 \cdot 10^3$
$\mathrm{ZZ} \to \mathrm{q\bar{q}q\bar{q}}$	$3.11 \cdot 10^2$	$1.74 \cdot 10^2$
$\mathrm{ZZ} \to \mathrm{q\bar{q}}\ell^+\ell^-$	$0.89 \cdot 10^2$	$4.97 \cdot 10^1$
$\mathrm{ZZ} \to \mathrm{q\bar{q}}\nu\bar{\nu}$	$1.78 \cdot 10^2$	$9.96 \cdot 10^1$
$\mathrm{q\bar{q}(q = u, d, s, c, b)}$	$1.29 \cdot 10^4$	$5.45 \cdot 10^3$
$\mathrm{We}\nu \to \mathrm{q\bar{q}e}\nu$	$5.08 \cdot 10^3$	$8.40 \cdot 10^3$
$\mathrm{Ze^+e^-} \to \mathrm{q\bar{q}e^+e^-}$	$4.46 \cdot 10^3$	$4.10 \cdot 10^3$

Table 2: Topological cross sections $\sigma \times BR$ of background processes at $\sqrt{s} = 500$, 800 GeV.

Cut	Tot. BG	ZZ	WW	2-ferm.	$t\bar{t}$	Eff.%	Signal
	9380780	157240	2087383	6799865	336290	100.0	13618
1	6035870	146909	1957360	3651766	279839	98.27	13383
2	2675300	105981	1309760	1047851	211705	91.34	12438
3	1357080	39789	383774	772600	160915	85.06	11583
4	335995	8167	50257	119448	158123	67.81	9235
5	306623	7832	48523	92288	157981	66.58	9067
6	265119	7499	46254	84886	126480	63.18	8604
7	148085	5975	35270	70218	36621	54.39	7407
8	41912	1761	809	10136	29206	53.22	7247
9	1960	272	19	473	1196	42.63	5805

Table 3: Number of remaining background events, signal efficiency and number of expected signal events after each of the nine cuts for the mass point (m_{H},m_{A}) = (150,100) in the $\mathrm{HA} \to \mathrm{b\bar{b}b\bar{b}}$ channel at $\sqrt{s} = 500$ GeV. The first column is the number of the cut, the second one is the number of total background events.

Cut	Tot. BG	ZZ	WW	2-ferm.	$t\bar{t}$	Eff.%	Signal
	4137520	87211	1183901	2783826	82579	100.0	3040
1	2376220	69491	922289	1307850	76592	97.00	2949
2	1007200	41522	462295	432605	70781	93.98	2857
3	542191	15305	154934	319818	52133	85.67	2604
4	90601	2328	21986	42023	24265	82.22	2499
5	78613	2117	20732	31502	24262	80.29	2441
6	54801	1937	16460	29276	7128	71.31	2168
7	12283	534	2075	4430	5244	68.99	2097
8	488	50	57	175	206	44.92	1366

Table 4: Number of remaining background events, signal efficiency and number of expected signal events after each of the eight cuts for the mass point $(m_{\mathrm{H}},m_{\mathrm{A}}) = (300,250)$ in the $\mathrm{HA} \to \mathrm{b\bar{b}b\bar{b}}$ channel at $\sqrt{s} = 800$ GeV. The first column is the number of the cut, the second one is the number of total background events.

$\sqrt{s}$ [GeV]	(m_{H},m_{A}) [GeV]	Efficiency [%]		Number of events		Tot. backgr.	
		cuts	2d.cut	cuts	2d.cut	cuts	2d.cut
500	(150,100)	43	31	5805	4196	1960	132
	(200,100)	41	26	4194	2661		129
	(250,100)	36	28	2422	1851		182
	(150,140)	48	39	5469	4518		301
	(150,150)	45	41	4944	4407		144
	(200,150)	42	27	3192	2036		130
	(250,150)	36	22	1534	960		156
	(200,200)	37	33	1691	1510		185
800	(300,150)	43	33	1825	1427	488	38
	(290,200)	46	36	1763	1398		53
	(300,250)	45	36	1366	1101		13
	(300,300)	44	35	1011	823		26
	(350,350)	37	31	339	277		58
	(400,150)	37	26	969	678		27
	(400,200)	40	28	833	584		41
	(400,250)	40	28	597	414		49

Table 5: The signal efficiencies, the number of signal and total background events after selection cuts and after cuts on di-jet mass sum and difference in the HA $\rightarrow \mathrm{b\bar{b}b\bar{b}}$ channel at $\sqrt{s} = 500$ and 800 GeV. The signal expectations are quoted for $\sin^2(\beta - \alpha) = 1$ and the Higgs boson branching fractions of $\mathrm{Br(H \rightarrow b\bar{b}) = Br(A \rightarrow b\bar{b})} = 90\%$.

$\sqrt{s}$ [GeV]	$(m_{\mathrm{H}},m_{\mathrm{A}})$ [GeV]	$\mathrm{HA} \rightarrow \mathrm{b\bar{b}}\tau^+\tau^-$		$\mathrm{HA} \rightarrow \tau^+\tau^-\mathrm{b\bar{b}}$		Tot.BG
		Eff.[%]	Events	Eff.[%]	Events	
500	(150,100)	68	1035	73	1110	133490
	(200,100)	67	765	72	820	
	(250,100)	61	460	70	525	
	(150,140)	73	940	73	940	
	(150,150)	74	900	74	900	
	(200,150)	70	595	71	605	
	(250,150)	63	305	70	340	
	(200,200)	69	355	69	355	
800	(300,150)	60	290	72	345	52020
	(290,200)	65	280	70	305	
	(300,250)	64	215	67	230	
	(300,300)	64	165	64	165	
	(350,350)	58	55	58	55	
	(400,150)	52	150	71	205	
	(400,200)	55	130	68	160	
	(400,250)	56	95	66	110	

Table 6: The $\mathrm{HA} \rightarrow \mathrm{b\bar{b}}\tau^+\tau^-$ and $\mathrm{HA} \rightarrow \tau^+\tau^-\mathrm{b\bar{b}}$ efficiencies, the number of signal and total background events after preselection at $\sqrt{s} = 500$ and 800 GeV. The signal expectations are quoted for $\sin^2(\beta-\alpha) = 1$ and the Higgs boson branching fractions of $\mathrm{Br}(\mathrm{H} \rightarrow \mathrm{b\bar{b}}) = \mathrm{Br}(\mathrm{A} \rightarrow \mathrm{b\bar{b}}) = 90\%$, $\mathrm{Br}(\mathrm{H} \rightarrow \tau\tau) = \mathrm{Br}(\mathrm{A} \rightarrow \tau\tau) = 10\%$.

$\sqrt{s}$ [GeV]	(m_{H},m_{A}) [GeV]	HA $\to$ $\mathrm{b\bar{b}}\tau^+\tau^-$		HA $\to$ $\tau^+\tau^-\mathrm{b\bar{b}}$		Tot.BG
		Eff.[%]	Events	Eff.[%]	Events	
500	(150,100)	42	640	44	670	5070
	(200,100)	39	445	42	480	5890
	(250,100)	21	160	28	210	2320
	(150,140)	41	525	42	540	3870
	(150,150)	42	510	42	510	4275
	(200,150)	34	290	38	325	2870
	(250,150)	30	145	35	170	3815
	(200,200)	29	150	29	150	2050
800	(300,150)	41	195	44	210	2023
	(290,200)	41	180	43	190	1350
	(300,250)	38	130	42	140	1056
	(300,300)	41	105	41	105	1609
	(350,350)	40	40	40	40	2632
	(400,150)	35	100	45	130	2528
	(400,200)	37	85	45	105	2430
	(400,250)	38	65	45	75	1842

Table 7: The HA $\to$ $\mathrm{b\bar{b}}\tau^+\tau^-$ and HA $\to$ $\tau^+\tau^-\mathrm{b\bar{b}}$ signal efficiencies and the number of signal and total background events accepted into the final samples at $\sqrt{s}$ = 500, 800 GeV. The signal expectations are quoted for $\sin(\beta-\alpha) = 1$ and the Higgs boson branching fractions of $\mathrm{Br(H \to b\bar{b}) = Br(A \to b\bar{b})}$ = 90%, $\mathrm{Br(H \to \tau\tau) = Br(A \to \tau\tau)}$ = 10%.

$\sqrt{s}$ [GeV]	$(m_{\rm H}, m_{\rm A})$ [GeV]	$\Delta m_{\rm H}$ [GeV]			$\Delta m_{\rm A}$ [GeV]		
		bbbb	$bb\tau^+\tau^-$	Comb.	bbbb	$bb\tau^+\tau^-$	Comb.
500	(150,100)	0.12	0.21	0.10	0.12	0.18	0.10
	(200,100)	0.15	0.45	0.14	0.15	0.30	0.13
	(250,100)	0.27	0.55	0.24	0.27	0.46	0.23
	(150,140)	0.13	0.28	0.12	0.13	0.25	0.12
	(150,150)	0.12	0.40	0.11	0.12	0.40	0.11
	(200,150)	0.26	0.58	0.24	0.26	0.40	0.22
	(250,150)	0.48	1.40	0.45	0.48	0.77	0.41
	(200,200)	0.31	1.30	0.30	0.31	1.30	0.30
800	(300,150)	0.33	0.44	0.26	0.33	0.57	0.29
	(290,200)	0.33	0.89	0.31	0.33	0.76	0.30
	(300,250)	0.45	1.08	0.42	0.45	1.02	0.41
	(300,300)	0.48	1.34	0.45	0.48	1.34	0.45
	(350,350)	0.97	2.12	0.88	0.97	1.12	0.73
	(400,150)	0.47	1.36	0.44	0.47	1.21	0.44
	(400,200)	0.74	2.00	0.69	0.74	1.88	0.69
	(400,250)	0.99	2.70	0.93	0.99	2.36	0.91

Table 8: Precision on the Higgs boson mass determination for the $b\bar{b}b\bar{b}$, $b\bar{b}\tau^+\tau^-$ channels and their combination at $\sqrt{s}$ = 500 and 800 GeV. Numbers are quoted for $\sin^2(\beta-\alpha) = 1$ and Higgs boson branching fractions of $\mathrm{Br}(\mathrm{H}\to b\bar{b}) = \mathrm{Br}(\mathrm{A}\to b\bar{b}) = 90\%$, $\mathrm{Br}(\mathrm{H}\to\tau\tau) = \mathrm{Br}(\mathrm{A}\to\tau\tau) = 10\%$.

$\sqrt{s}$ [GeV]	$(m_{\rm H}, m_{\rm A})$ [GeV]	$\Delta\sigma/\sigma$ [%]		
		HA $\rightarrow$ bbbb	HA $\rightarrow$ bb$\tau^+\tau^-$	HA $\rightarrow$ $\tau^+\tau^-$bb
500	(150,100)	1.6	5.2	4.9
	(200,100)	2.0	7.5	5.8
	(250,100)	2.4	16.3	8.9
	(150,140)	1.5	7.2	6.3
	(150,150)	1.5	4.2	4.2
	(200,150)	2.3	9.7	8.7
	(250,150)	3.5	22.6	13.5
	(200,200)	2.7	8.1	8.1
800	(300,150)	2.7	10.0	8.8
	(290,200)	2.7	11.2	10.9
	(300,250)	3.0	13.8	11.9
	(300,300)	3.5	10.0	10.0
	(350,350)	6.6	17.0	17.0
	(400,150)	3.9	16.3	11.6
	(400,200)	4.3	21.5	19.8
	(400,250)	5.2	31.7	28.5

Table 9: Relative uncertainty in the topological cross section measurements for the $b\bar{b}b\bar{b}$, $b\bar{b}\tau^+\tau^-$ channels at $\sqrt{s}$ = 500 and 800 GeV. Numbers are quoted for $\sin^2(\beta-\alpha) = 1$ and the Higgs boson branching fractions of $\rm Br(H \rightarrow b\bar{b}) = Br(A \rightarrow b\bar{b}) = 90\%$, $\rm Br(H \rightarrow \tau\tau) = Br(A \rightarrow \tau\tau) = 10\%$.

$(m_{\mathrm{H}}, m_{\mathrm{A}})$ [GeV]	$\Gamma_{\mathrm{H,A}}$ [GeV]	$\delta\Gamma_{\mathrm{H}}$ [GeV]	$\delta\Gamma_{\mathrm{A}}$ [GeV]
(150,100)	0	<0.9	<0.9
	5	$^{-0.6}_{+1.3}$	$^{-0.6}_{+1.3}$
	10	$^{-1.3}_{+1.6}$	$^{-1.1}_{+1.6}$
(200,150)	0	<1.7	<1.8
	5	$^{-1.1}_{+2.1}$	$^{-1.2}_{+2.1}$
	10	$^{-2.0}_{+2.6}$	$^{-2.0}_{+3.0}$
(300,250)	0	<3.6	<3.6
	5	$^{-2.5}_{+2.9}$	$^{-2.5}_{+2.9}$
	10	$^{-2.9}_{+3.6}$	$^{-2.8}_{+4.0}$

Table 10: The accuracy of the Higgs boson width measurements in the case of large mass splitting between Higgs bosons. The upper limits on the Higgs boson width in the case of $\Gamma_{\mathrm{H}} = \Gamma_{\mathrm{A}} = 0$ GeV correspond to 95% confidence level.

$(m_{\mathrm{H}}, m_{\mathrm{A}})$ [GeV]	$\Gamma_{\mathrm{H,A}}$ [GeV]	$\delta\Gamma_{\mathrm{H,A}}$ [GeV]
(150,150)	0	<1.4
	5	$^{-1.0}_{+1.4}$
	10	$^{-1.7}_{+2.1}$
(200,200)	0	<3.3
	5	$^{-2.0}_{+2.5}$
	10	$^{-3.2}_{+3.7}$
(300,300)	0	<4.5
	5	$^{-3.2}_{+3.7}$
	10	$^{-4.0}_{+4.5}$

Table 11: The accuracy on the Higgs boson width measurements in the case of Higgs boson mass degeneracy. The upper limits on the Higgs boson width in the case of $\Gamma_{\mathrm{H}} = \Gamma_{\mathrm{A}} = 0$ GeV correspond to 95% confidence level.

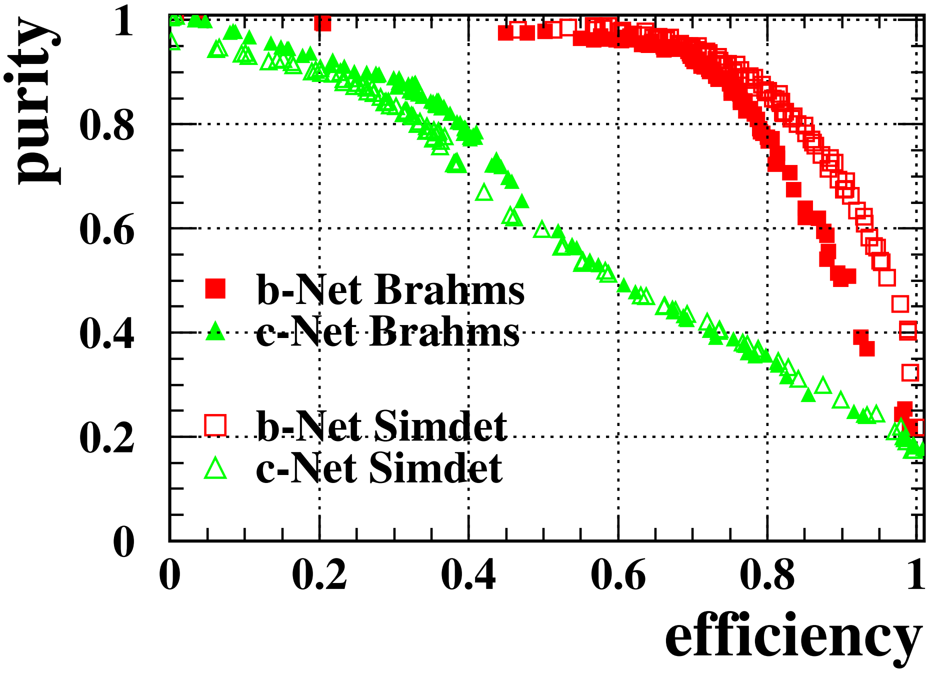

Figure 1: b-tag and the c-tag purity of the neural network (Section 4.1) versus efficiency curves for $Z \rightarrow q\bar{q}$ events simulated with SIMDET and BRAHMS at a center-of-mass energy of $\sqrt{s} = 91.2\,\mathrm{GeV}$. Filled squares (triangles) correspond to the neural network output for the b-events (c-events) simulated with BRAHMS. Open squares (triangles) correspond to the neural network output for the b-events (c-events) simulated with SIMDET. The neural networks are trained on event samples simulated with SIMDET using the same variables and jet classification as in BRAHMS.

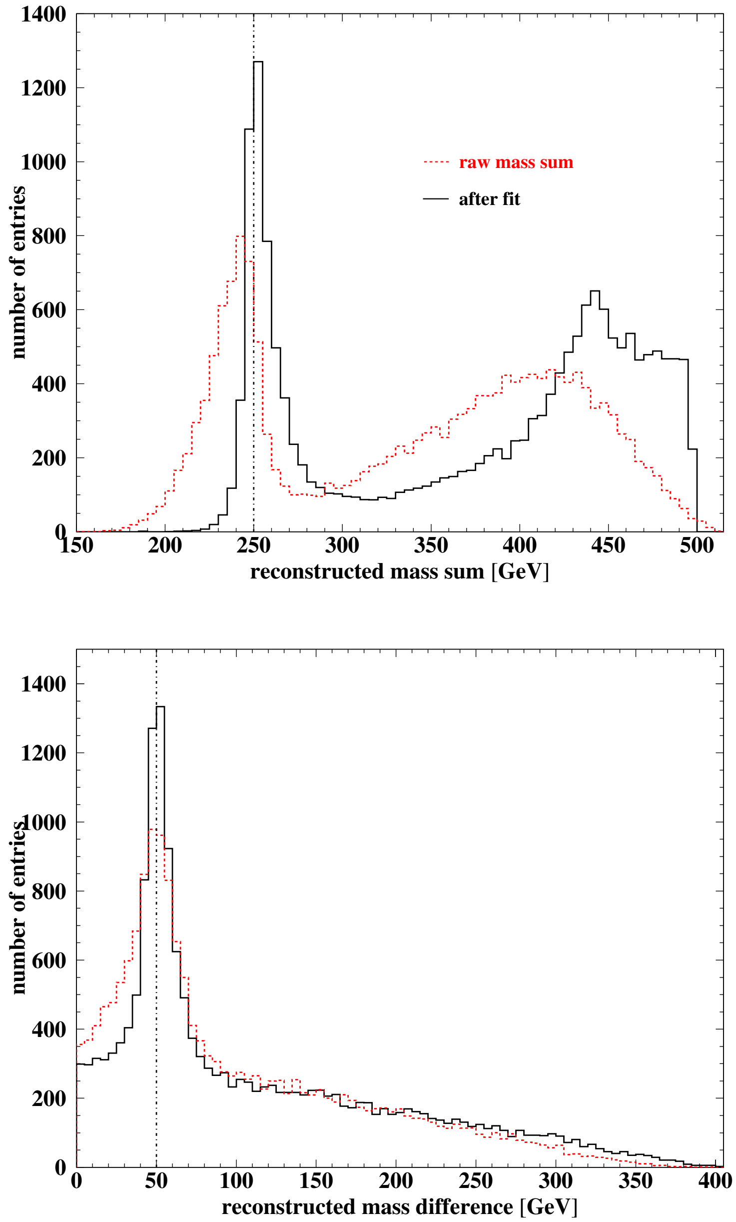

Figure 2: Distributions of the reconstructed invariant mass sum (upper figure) and mass difference (lower figure) in the sample of the HA $\rightarrow$ b$\bar{\text{b}}$b$\bar{\text{b}}$ events with $(m_{\text{H}}, m_{\text{A}})$ = (150,100) GeV at $\sqrt{s} = 500\,\text{GeV}$. Dashed histograms show raw spectra obtained using only measured jet angles and energies. Solid histograms show spectra obtained after applying 4C kinematic fit. Three entries per event contribute to distributions, corresponding to three possible di-jet pairings.

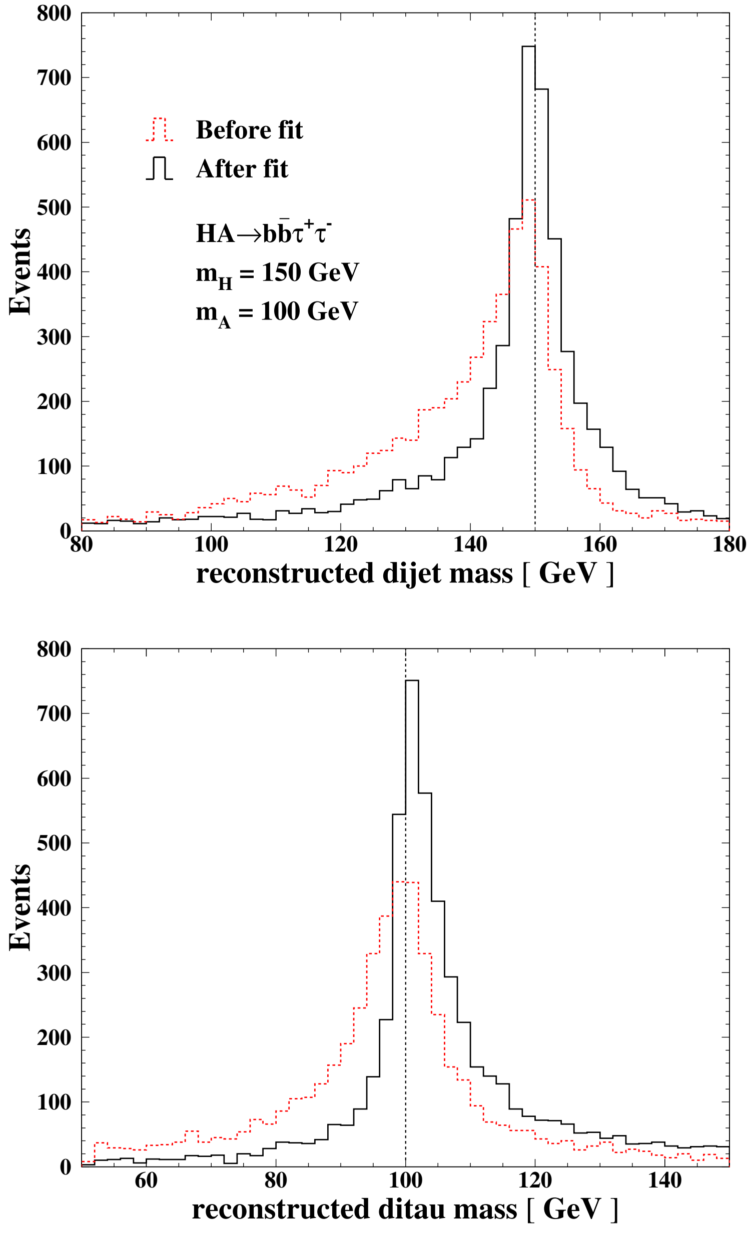

Figure 3: The mass spectrum of the di-jet (upper figure) and di-tau (lower figure) systems in the sample of the HA $\to$ b$\bar{\mathrm{b}}\tau^+\tau^-$ events with $(m_{\mathrm{H}},m_{\mathrm{A}}) =$ (150,100) GeV at $\sqrt{s} = 500\,\mathrm{GeV}$. Dashed histograms represent distributions before applying kinematic fit, solid - after applying kinematic fit.

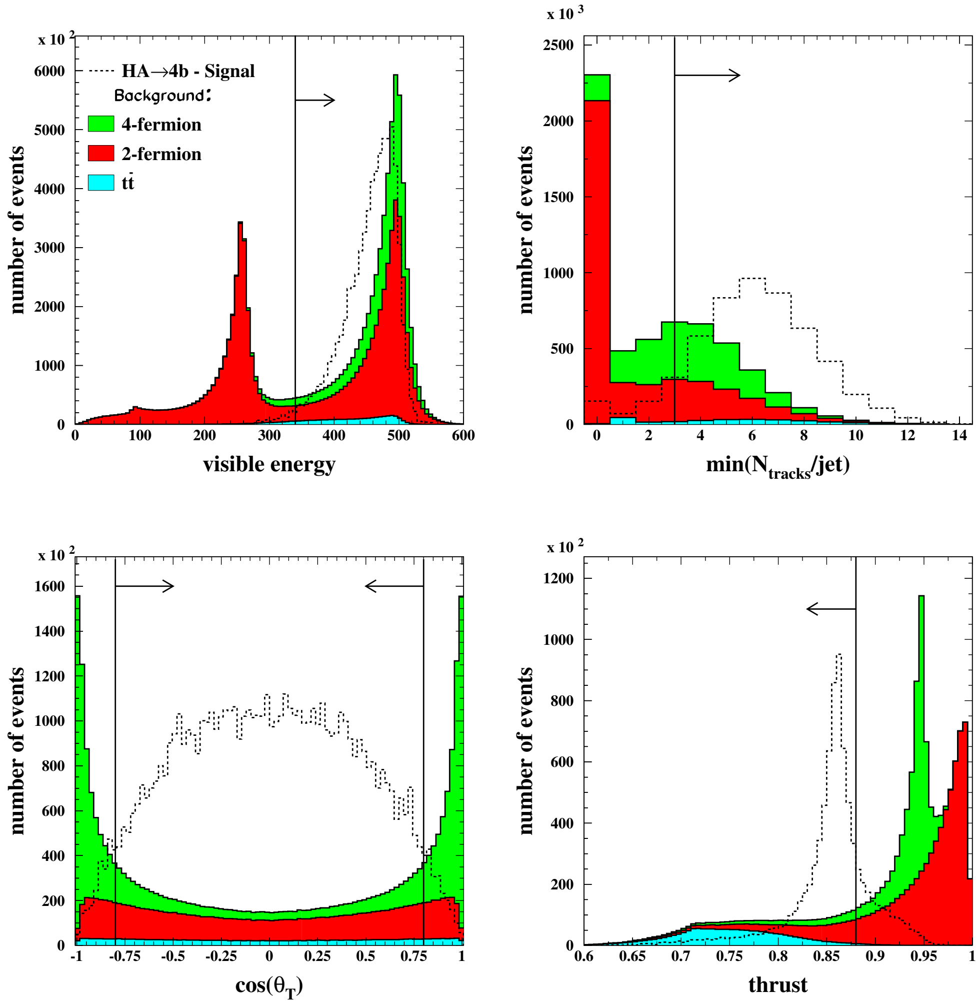

Figure 4: Distributions of the selection variables (visible energy, number of tracks per jet N_{tracks}/jet, $\cos\theta_T$ and a thrust value) in the HA $\rightarrow$ $\mathrm{b\bar{b}b\bar{b}}$ channel with $(m_{\mathrm{H}},m_{\mathrm{A}})$ = (150,100) GeV at $\sqrt{s}$ = 500 GeV. The signal distributions are shown with arbitrary normalisation. The vertical lines and arrows indicate cuts, imposed on these variables. The distributions are shown after all cuts preceding the current variable.

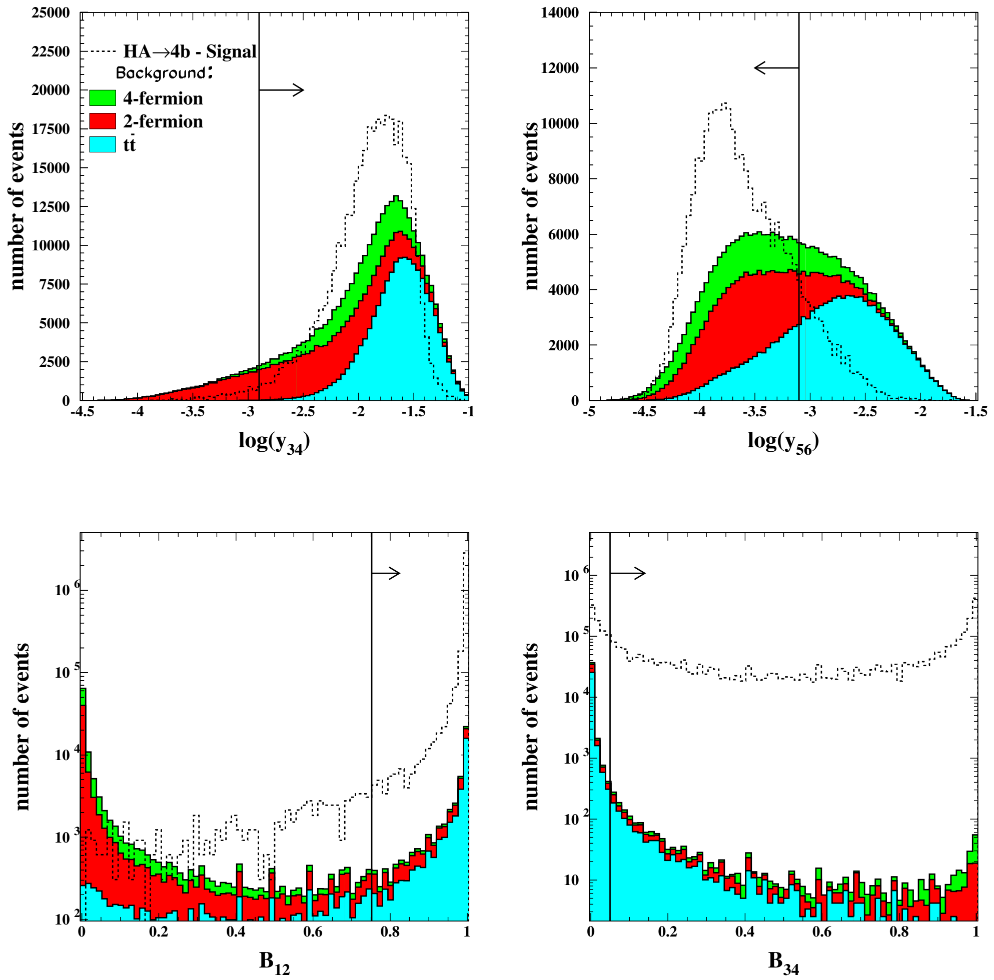

Figure 5: Distributions of the selection variables (jet resolution parameters $\log_{10} y_{34}$ and $\log_{10} y_{56}$ and b-tag variables B_{12} and B_{34}) in the $\mathrm{HA} \rightarrow \mathrm{b\bar{b}b\bar{b}}$ channel with $(m_{\mathrm{H}}, m_{\mathrm{A}}) = (150{,}100)$ GeV at $\sqrt{s} = 500$ GeV. The signal distributions are shown with arbitrary normalisation. The vertical lines and arrows indicate cuts, imposed on these variables. The distributions are shown after all cuts preceding the current variable.

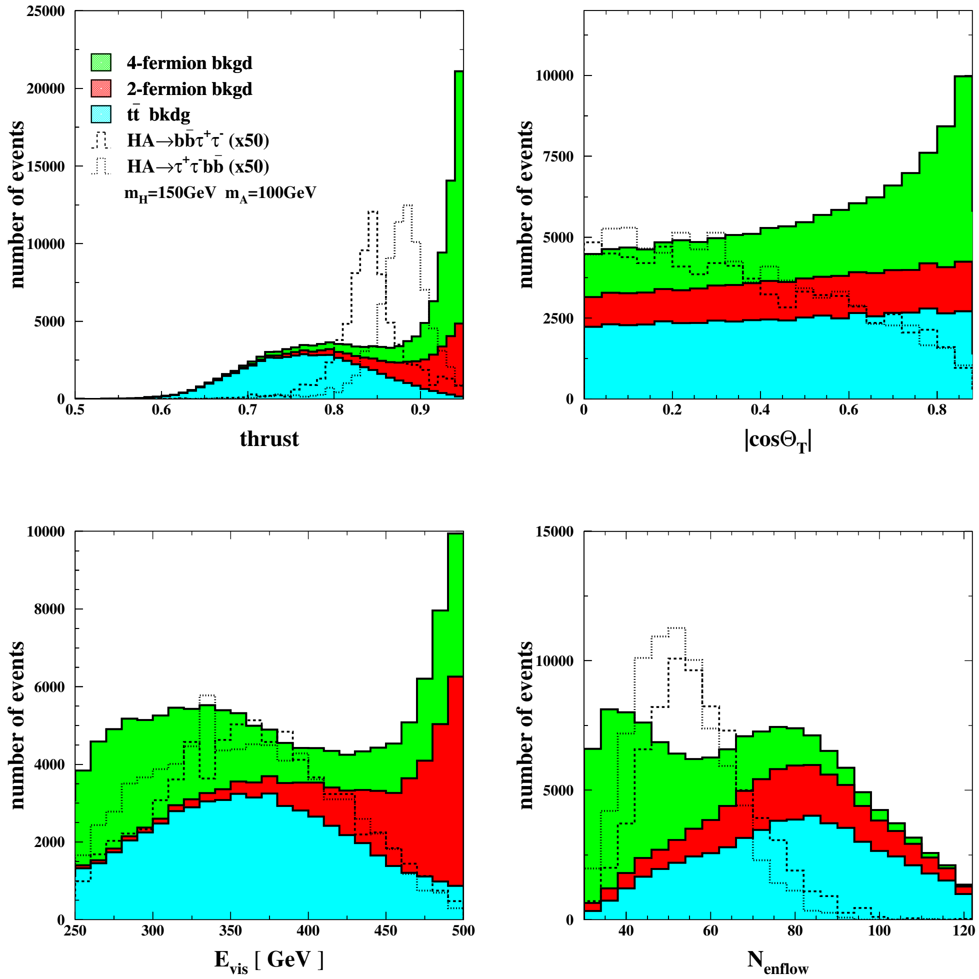

Figure 6: Variables used to construct signal likelihood (thrust value, $\cos\theta_T$, visible energy E_{vis} and number of energy flow objects N_{enflow}) in the HA $\rightarrow \mathrm{b\bar{b}}\tau^+\tau^-, \tau^+\tau^-\mathrm{b\bar{b}}$ channels with $(m_{\mathrm{H}},m_{\mathrm{A}})$ = (150,100) GeV at $\sqrt{s}$ = 500 GeV. The distributions are shown after cuts 1-6 (Section 5.2).

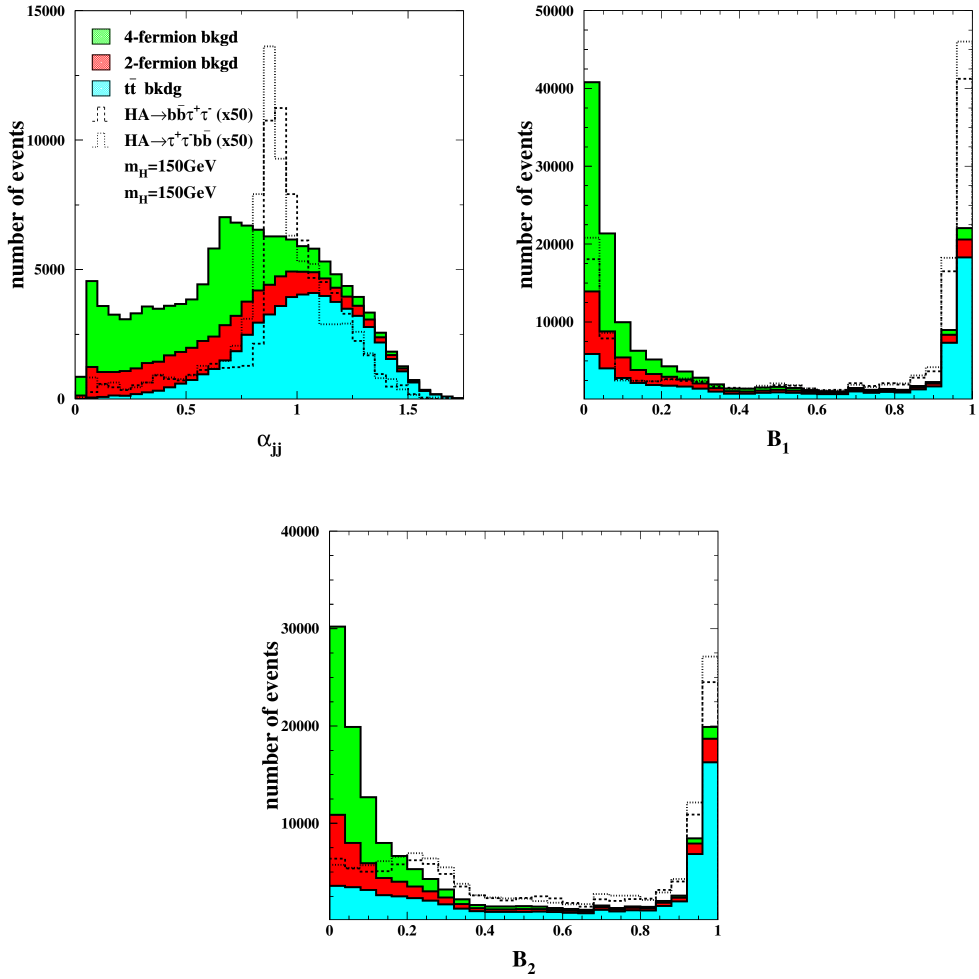

Figure 7: Variables used to construct signal likelihood (minimal opening angle between any two jets α_{jj} and b-tag variables B_1 and B_2) in the HA $\rightarrow$ b$\bar{\text{b}}\tau^+\tau^-, \tau^+\tau^-b\bar{\text{b}}$ channels with $(m_{\text{H}}, m_{\text{A}})$ = (150,100) GeV at $\sqrt{s}$ = 500 GeV. The distributions are shown after cuts 1-6 (Section 5.2).

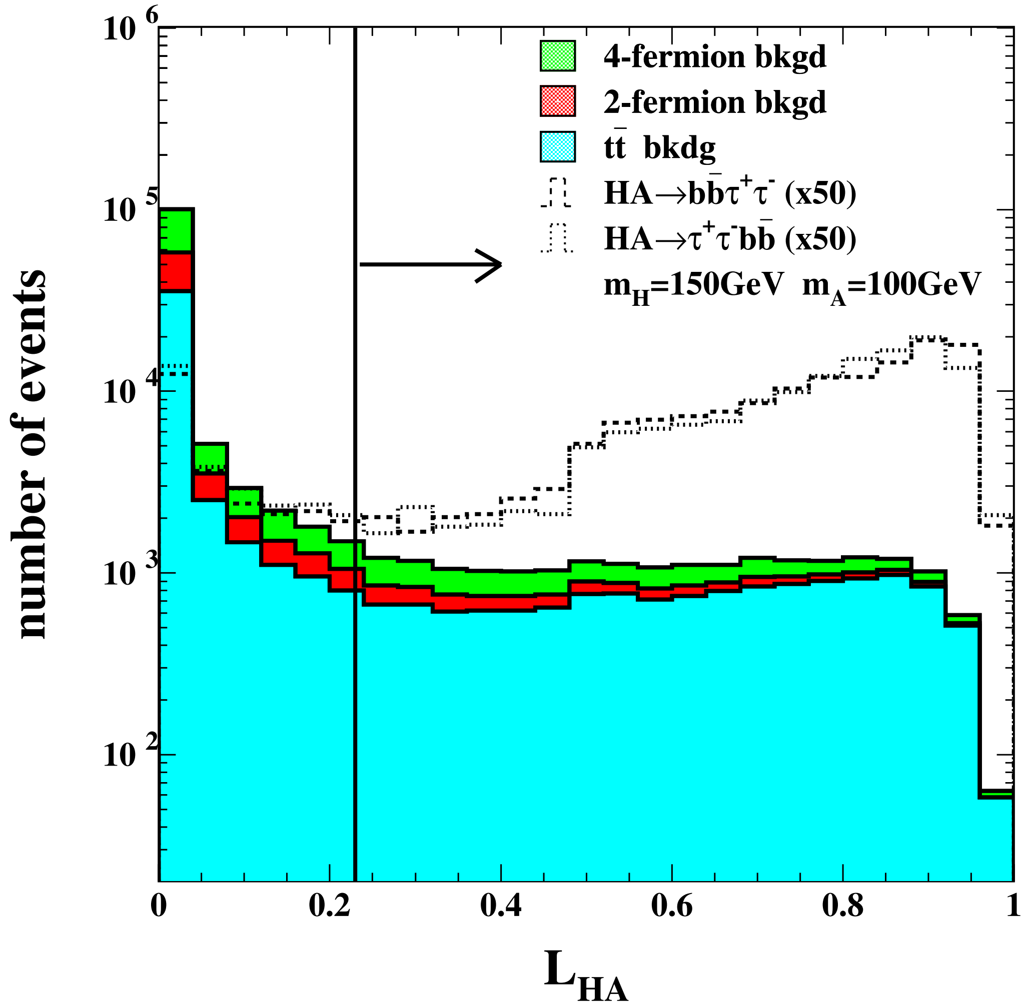

Figure 8: Distribution of L_{HA} in the HA $\rightarrow$ b$\bar{b}\tau^+\tau^-$, $\tau^+\tau^-$b$\bar{b}$ channels with $(m_H, m_A) = (150,100)$ GeV at $\sqrt{s} = 500$ GeV. The vertical line and arrow indicate cut placed on the likelihood.

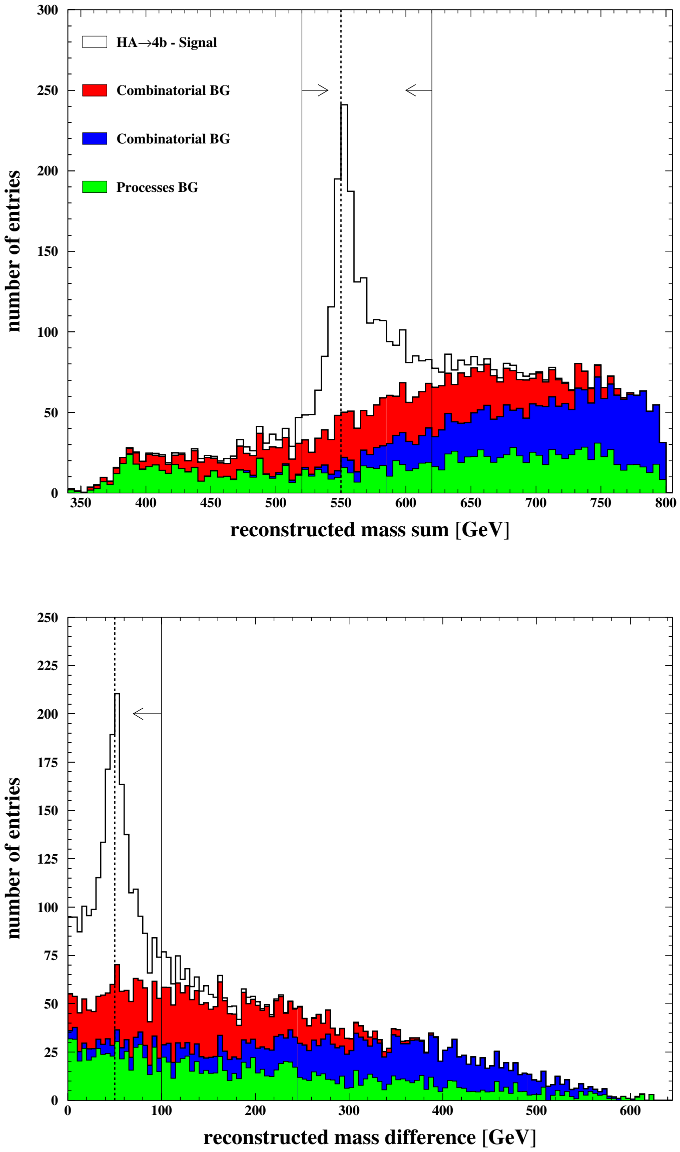

Figure 9: Distributions of the di-jet mass sum (upper figure) and di-jet mass difference (lower figure) in the HA $\rightarrow$ b$\bar{\text{b}}$b$\bar{\text{b}}$ channel for Higgs boson mass hypothesis (m_{H},m_{A}) = (300,250) GeV at $\sqrt{s}$ = 800 GeV after selection cuts and kinematic fit. The three components of the signal are shown separately: two combinatorial parts and one of the real signal. The background from the other processes is presented as well.

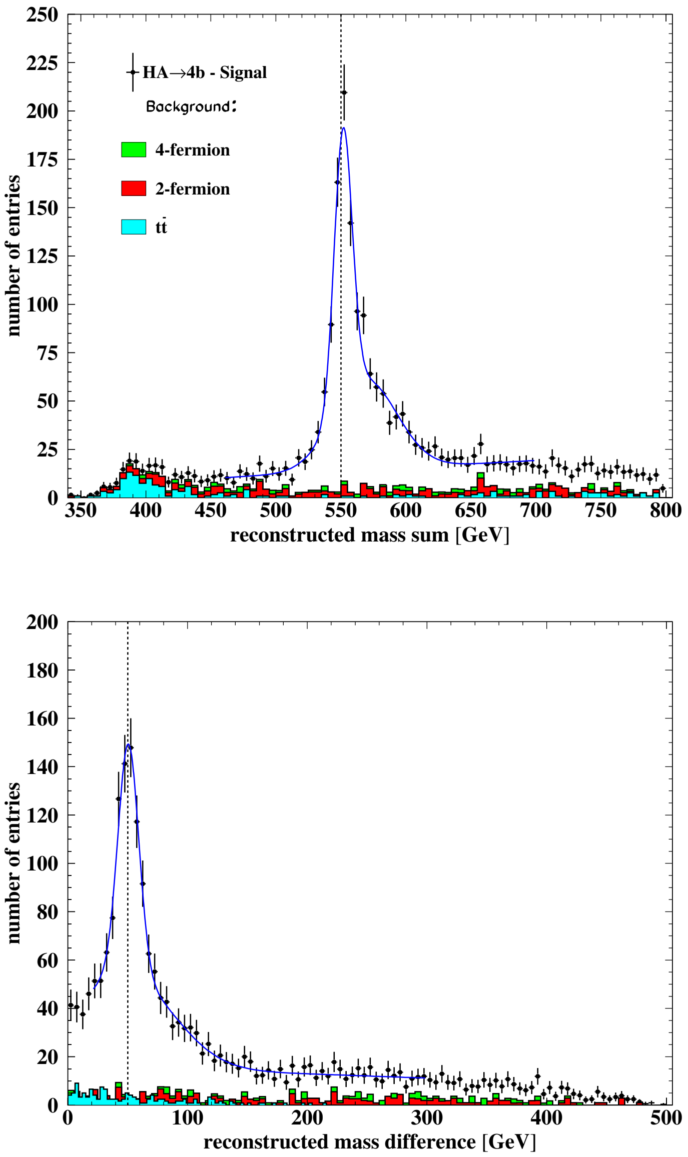

Figure 10: Upper figure: distribution of the di-jet mass sum after selection cuts, kinematic fit and cut on di-jet mass difference. Lower figure: distribution of the di-jet mass difference after selection cuts, kinematic fit and cut on di-jet mass sum. Both distributions are in the HA $\rightarrow$ $\mathrm{b\bar{b}b\bar{b}}$ channel for the Higgs boson mass hypothesis $(m_{\mathrm{H}},m_{\mathrm{A}}) = (300{,}250)$ GeV at $\sqrt{s} = 800$ GeV.

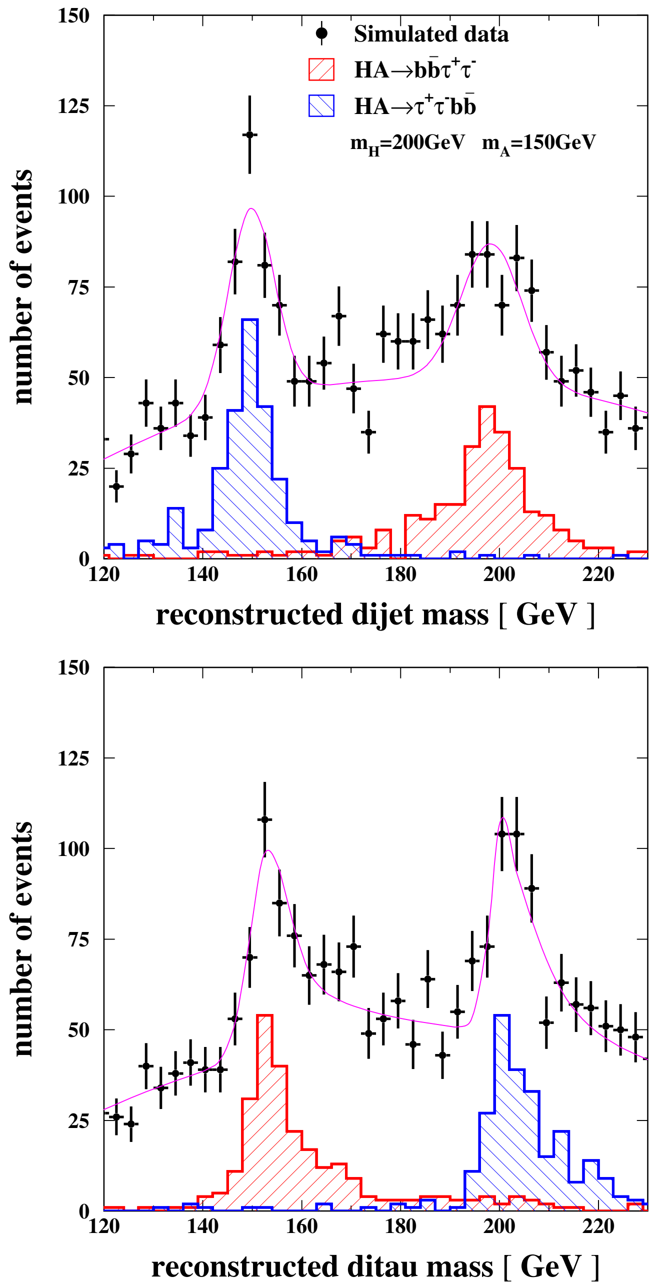

Figure 11: Distributions of di-jet mass and di-tau mass in the $\mathrm{HA} \to \mathrm{b\bar{b}}\tau^+\tau^-, \tau^+\tau^-\mathrm{b\bar{b}}$ channels for the case of $(m_{\mathrm{H}},m_{\mathrm{A}})$ = (200,150) GeV at $\sqrt{s}$ = 500 GeV.

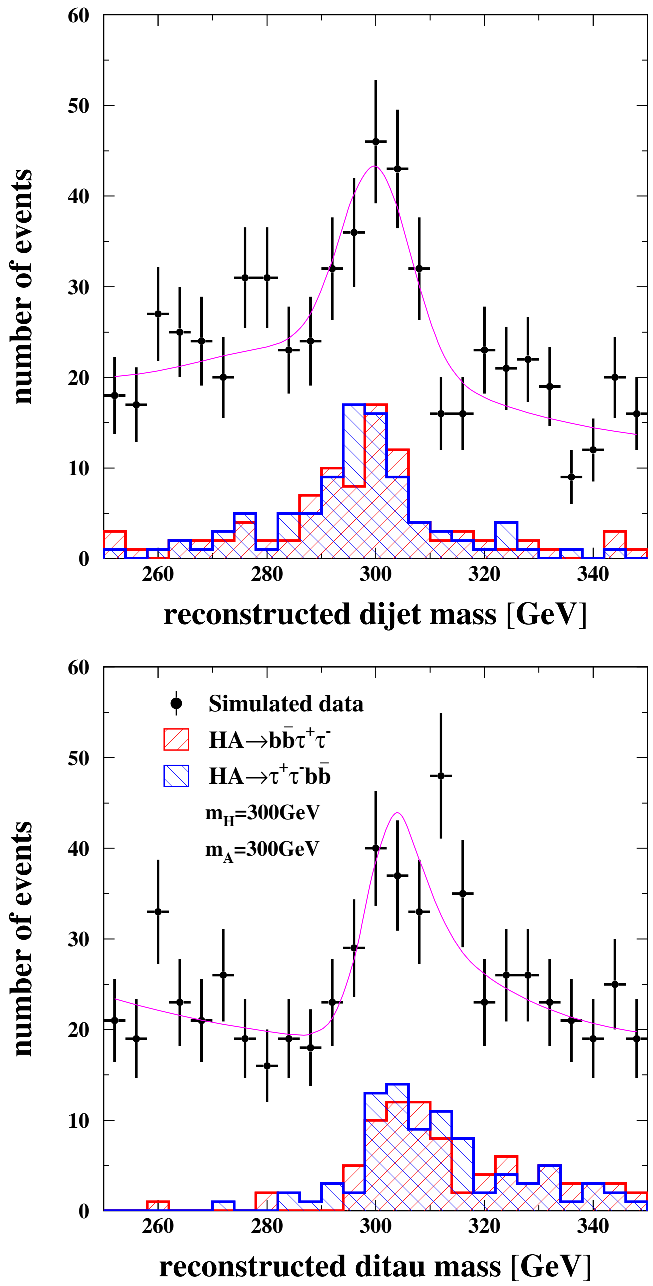

Figure 12: Distributions of di-jet mass and di-tau mass in the HA $\to \mathrm{b\bar{b}}\tau^+\tau^-, \tau^+\tau^-\mathrm{b\bar{b}}$ channels for the case of $(m_{\mathrm{H}}, m_{\mathrm{A}})$ = (300,300) GeV at $\sqrt{s} = 800$ GeV.

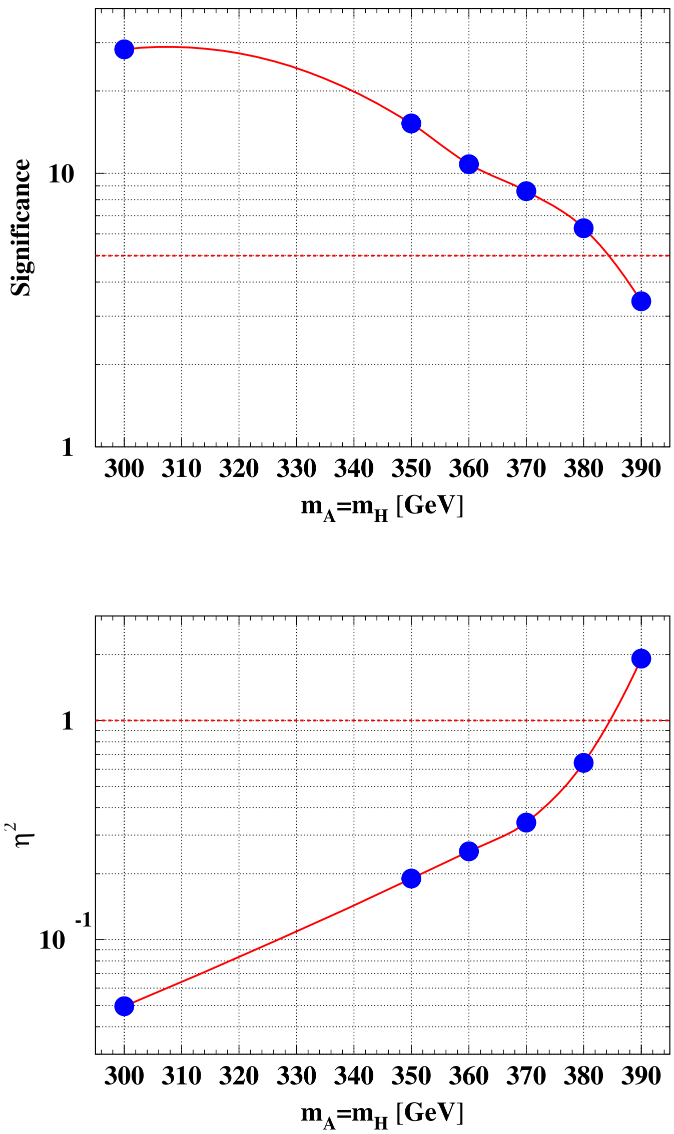

Figure 13: Discovery significance as a function of the Higgs boson mass (assuming $m_H = m_A$) in the HA $\rightarrow$ $b\bar{b}b\bar{b}$ channel at $\sqrt{s} = 800$ GeV (upper figure). η^2 as a function of the Higgs boson mass for the 5σ discovery limit (lower figure) where η^2 is assumed $e^+e^- \rightarrow$ HA cross section relative to that for $\sin^2(\beta - \alpha) = 1$. Branching ratios Br(H $\rightarrow b\bar{b}$) and Br(A $\rightarrow b\bar{b}$) are assumed to be 90%.

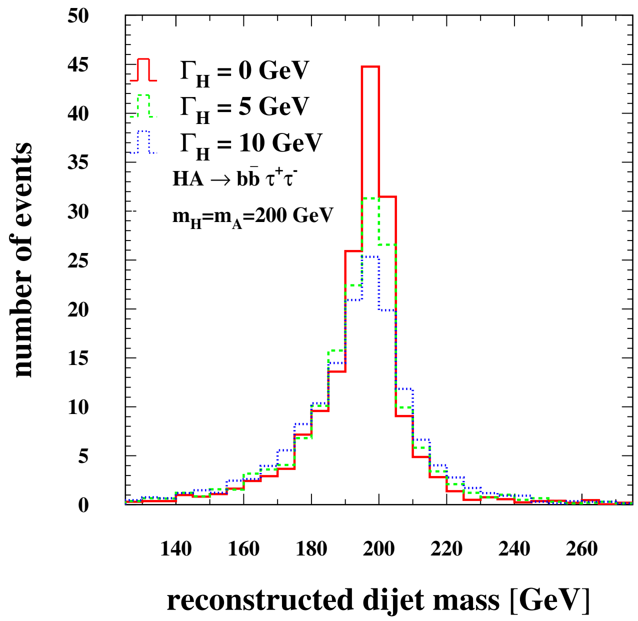

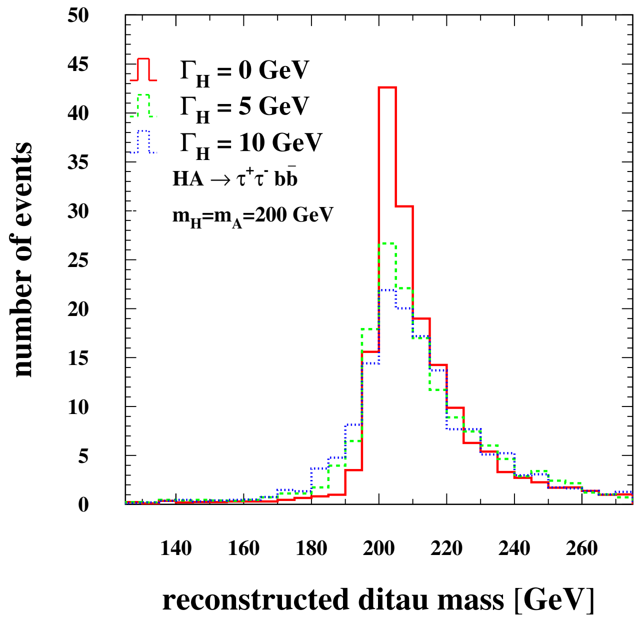

Figure 14: The reconstructed di-jet mass spectrum in the HA $\to$ b$\bar{\text{b}}\tau^+\tau^-$ sample (upper figure) and the reconstructed di-tau mass spectrum in the HA $\to \tau^+\tau^-$b$\bar{\text{b}}$ sample (lower figure) for the different Higgs boson widths $\Gamma_{\rm H}$ = 0, 5, 10 GeV for $m_{H,A}$ = 200 GeV at $\sqrt{s}$ = 500 GeV.

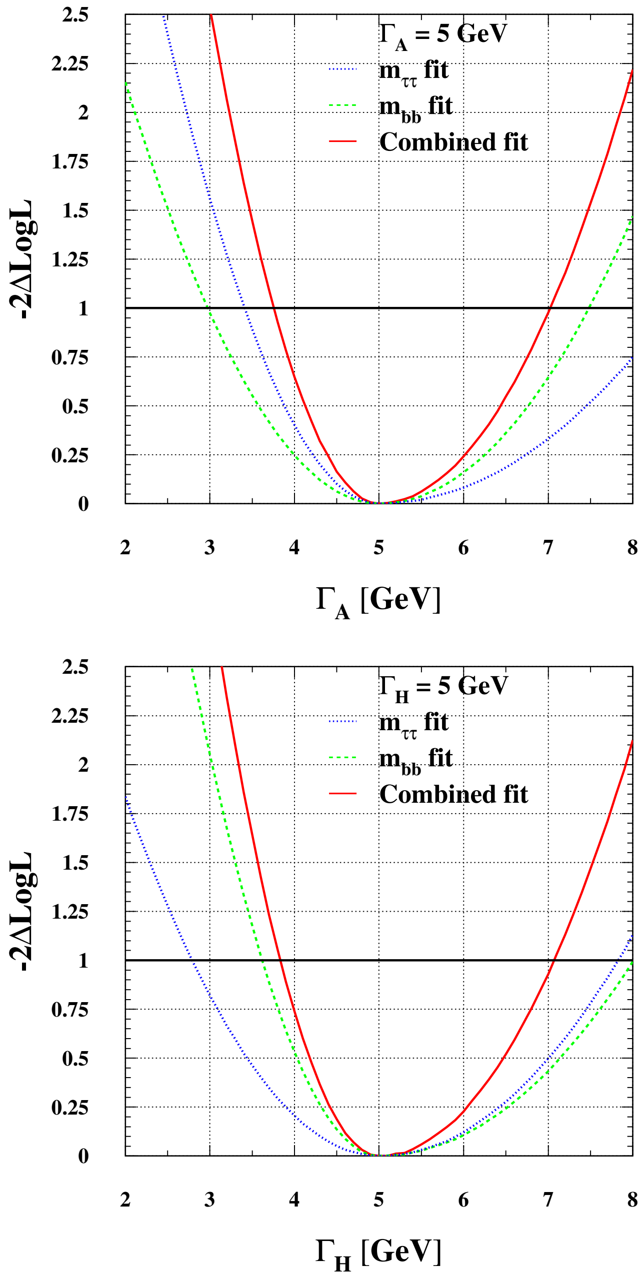

Figure 15: The log-likelihood as a function of Γ_H and Γ_A for the case of $\Gamma_H = \Gamma_A = 5$ GeV and $(m_H, m_A) = (200, 150)$ GeV at $\sqrt{s} = 500$ GeV.

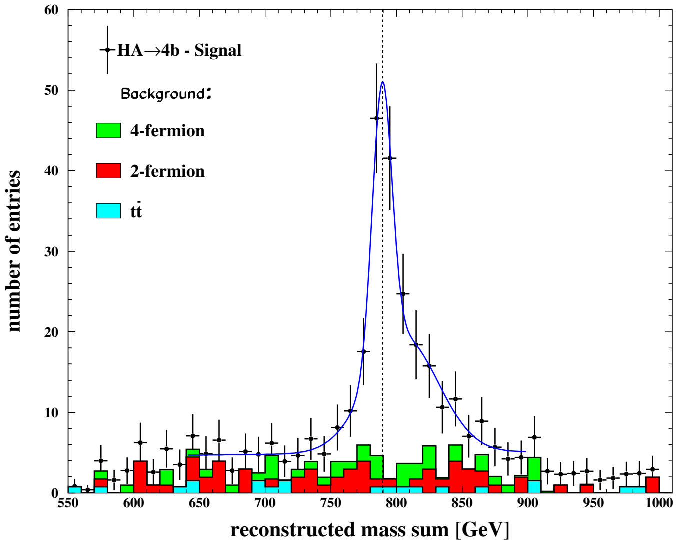

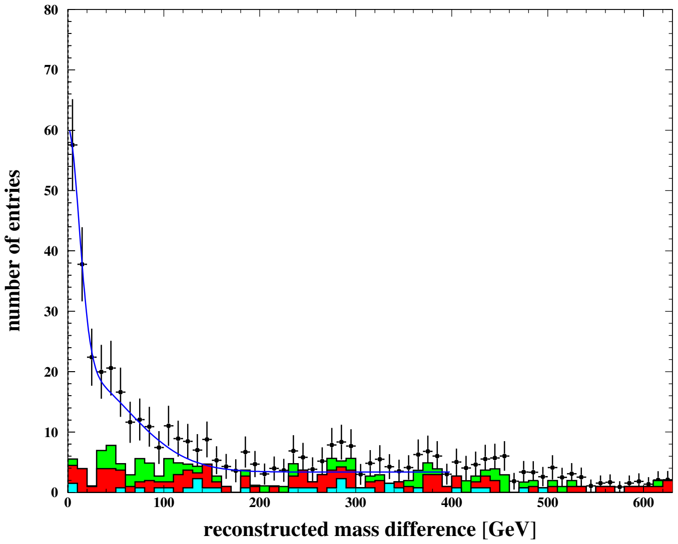

Figure 16: Upper figure: distribution of the di-jet mass sum after selection cuts, kinematic fit and cut on di-jet mass difference. Lower figure: distribution of the di-jet mass difference after selection cuts, kinematic fit and cut on di-jet mass sum. Both distributions are in the HA $\rightarrow$ $\mathrm{b\bar{b}b\bar{b}}$ channel for the SPS 1a benchmark point with Higgs boson mass hypothesis (m_{H},m_{A}) = (394.90,394.65) GeV at $\sqrt{s}$ = 1 TeV.